

Toward A Globally-Applicable Uncertainty Quantification Framework for Satellite Multisensor Precipitation Products based on GPM DPR

Zhe Li¹, Daniel Wright¹, Samantha Hartke¹, Dalia Kirschbaum², Sana Khan³, Viviana Maggioni⁴, and Pierre-Emmanuel Kirstetter⁵

¹Department of Civil and Environmental Engineering, University of Wisconsin–Madison, Madison, WI, USA

²NASA

³NASA Goddard Space Flight Center

⁴George Mason University

⁵University of Oklahoma, National Severe Storms Laboratory

November 26, 2022

Abstract

The usefulness of satellite multisensor precipitation products such as NASA’s 30-minute, 0.1° Integrated Multi-satellitE Retrievals for the Global Precipitation Mission (IMERG) is hindered by their associated errors. Reliable estimates of uncertainty would mitigate this limitation, especially in near-real time. Creating such estimates is challenging, however, due both to the complex discrete-continuous nature of satellite precipitation errors and to the lack of “ground truth” data precisely in the places—including complex terrain and developing countries—that could benefit most from satellite precipitation estimates. In this work, we use swath-based precipitation products from the Global Precipitation Mission (GPM) Dual-frequency Precipitation Radar (DPR) as an alternative to ground-based observations to facilitate IMERG uncertainty estimation. We compare the suitability of two DPR derived products, 2ADPR and 2BCMB, against higher-fidelity Ground Validation Multi-Radar Multi-Sensor (GV-MRMS) ground reference data over the contiguous United States. 2BCMB is selected to train mixed discrete-continuous error models based on Censored Shifted Gamma Distributions. Uncertainty estimates from these error models are compared against alternative models trained on GV-MRMS. Using information from NASA’s Modern-Era Retrospective analysis for Research and Applications, Version 2 (MERRA-2) reanalysis, we also demonstrate how IMERG uncertainty estimates can be further constrained using additional precipitation-related predictors. Though several critical issues remain unresolved, the proposed method shows promise for yielding robust uncertainty estimates in near-real time for IMERG and other similar precipitation products at their native resolution across the entire globe.

1 **Toward A Globally-Applicable Uncertainty Quantification Framework**
2 **for Satellite Multisensor Precipitation Products based on GPM DPR**
3

4
5 **Zhe Li¹, Daniel B. Wright¹, Samantha H. Hartke¹, Dalia B. Kirschbaum², Sana Khan^{2,3},**
6 **Viviana Maggioni⁴, Pierre-Emmanuel Kirstetter^{5,6}**

7 ¹Department of Civil and Environmental Engineering, University of Wisconsin–Madison,
8 Madison, WI, USA

9 ²NASA Goddard Space Flight Center, Greenbelt, MD, USA

10 ³Earth System Science Interdisciplinary Center, University of Maryland, MD, USA

11 ⁴Civil, Infrastructure and Environmental Engineering Department, George Mason University,
12 Fairfax, VA, USA

13 ⁵School of Meteorology and School of Civil Engineering and Environmental Science, University
14 of Oklahoma, Norman, OK, USA

15 ⁶NOAA/National Severe Storms Laboratory, Norman, OK, USA
16

17
18
19
20 Version: JUNE 07, 2021
21
22
23
24
25
26
27

28 Corresponding author: Dr. Zhe Li (zli875@wisc.edu)

29 *Department of Civil and Environmental Engineering, University of Wisconsin-Madison,*
30 *1221 Engineering Hall, 1415 Engineering Drive, Madison, WI 53706, USA*

31 **Key Points:**

- 32 • We propose a globally-applicable uncertainty quantification framework for satellite
33 precipitation products at their native resolution
- 34 • The framework performs well over the contiguous United States for according to both
35 deterministic and probabilistic evaluation metrics
- 36 • The framework's uncertainty estimates can be further constrained using additional
37 precipitation-related predictors

38
39
40
41
42
43
44
45
46
47
48
49
50
51
52
53

54
55
56
57
58
59
60
61
62
63
64
65
66
67
68
69
70
71
72
73**Abstract**

The usefulness of satellite multisensor precipitation products such as NASA’s 30-minute, 0.1° Integrated Multi-satellitE Retrievals for the Global Precipitation Mission (IMERG) is hindered by their associated errors. Reliable estimates of uncertainty would mitigate this limitation, especially in near-real time. Creating such estimates is challenging, however, due both to the complex discrete-continuous nature of satellite precipitation errors and to the lack of “ground truth” data precisely in the places—including complex terrain and developing countries—that could benefit most from satellite precipitation estimates. In this work, we use swath-based precipitation products from the Global Precipitation Mission (GPM) Dual-frequency Precipitation Radar (DPR) as an alternative to ground-based observations to facilitate IMERG uncertainty estimation. We compare the suitability of two DPR derived products, 2ADPR and 2BCMB, against higher-fidelity Ground Validation Multi-Radar Multi-Sensor (GV-MRMS) ground reference data over the contiguous United States. 2BCMB is selected to train mixed discrete-continuous error models based on Censored Shifted Gamma Distributions. Uncertainty estimates from these error models are compared against alternative models trained on GV-MRMS. Using information from NASA’s Modern-Era Retrospective analysis for Research and Applications, Version 2 (MERRA-2) reanalysis, we also demonstrate how IMERG uncertainty estimates can be further constrained using additional precipitation-related predictors. Though several critical issues remain unresolved, the proposed method shows promise for yielding robust uncertainty estimates in near-real time for IMERG and other similar precipitation products at their native resolution across the entire globe.

74 **1 Introduction**

75 The potential of satellite precipitation estimates to understand and predict global-to-regional
76 water cycles has been recognized for decades (Kidd et al., 2020; Lettenmaier et al., 2015;
77 Skofronick-Jackson et al., 2018). Due to the limited number and uneven distribution of rain gauges
78 that accurately measure precipitation on the ground (e.g., Kidd et al., 2017), global satellite multi-
79 sensor precipitation (SMP) products have been increasingly applied to support decision-making,
80 particularly in data-sparse regions such as the oceans, mountainous areas, and developing countries
81 (e.g., Kirschbaum et al., 2017; Wright, 2018).

82 SMP products generally merge measurements from passive microwave (PMW) and infrared
83 (IR) sensors to create consistent high-resolution gridded precipitation estimates (Li et al., 2020;
84 Maggioni et al., 2016; Sun et al., 2018). A number of global SMP products have been developed
85 based on different merging techniques, including the NASA's Integrated Multisatellite Retrievals
86 for Global Precipitation Measurements (IMERG; Huffman et al., 2019), and its predecessor—the
87 Tropical Rainfall Measuring Mission Multisatellite Precipitation Analysis (TMPA; Huffman et al.,
88 2007), the Climate Prediction Center morphing technique (CMORPH; Joyce et al., 2004; Joyce &
89 Xie, 2011), and the Remotely Sensed Information Using Artificial Neural Networks (PERSIANN)
90 family (Nguyen et al., 2018; Sorooshian et al., 2000).

91 Despite continual improvements, the usefulness of SMP products remains limited due to their
92 oftentimes poor accuracy (e.g., Foufoula-Georgiou et al., 2020; Massari & Maggioni, 2020). These
93 errors stem from a variety of sources, including heterogeneous sensor properties (Guilloteau et al.,
94 2017; Tan et al., 2016), retrieval algorithm deficiencies (Kirstetter et al., 2020), and insufficient

95 spatial and temporal sampling (Behrangi & Wen, 2017; Kidd & Maggioni, 2020). The absolute
96 and relative roles of these error sources can depend on season, precipitation intensity, storm type,
97 geophysical features such as latitude and land surface type, and other factors (Ebert et al., 2007;
98 Gebregiorgis & Hossain, 2014; Gebregiorgis et al., 2017; Kirstetter et al., 2018).

99 A large number of existing studies have presented empirical characterizations of SMP error
100 using “ground truth”, i.e., more reliable reference observations (typically rain gauges or gauge-
101 corrected weather radar; see Kirstetter et al., 2012; Massari & Maggioni, 2020 for a discussion).
102 Errors are often separated into systematic (i.e., bias) and random error components (AghaKouchak
103 et al., 2012; Tang, 2020; Tian et al., 2013). These errors typically depend on precipitation
104 magnitude via conditional bias (heteroscedasticity) in the case of systematic (random) error (e.g.,
105 Massari & Maggioni, 2020). Other approaches have considered additional terms to characterize
106 errors in both detection and magnitude estimation, distinguishing between “false alarm”
107 precipitation, missed precipitation, and hit bias (e.g., Tian et al., 2009). These studies have always
108 been undertaken at local to regional scales due to the lack of sufficient ground reference globally
109 (e.g., Beck et al., 2019; Li et al., 2013; O et al., 2017; Tang et al., 2016). Unfortunately, however,
110 lessons learned in such studies cannot be easily transferred to other places due to the complexity
111 of satellite precipitation uncertainties (Kidd & Maggioni, 2020; Tang & Hossain, 2012).

112 Furthermore, ex-post SMP error studies are not sufficient to meet uncertainty characterization
113 requirements for applications, particularly those in near-realtime. Such a requirement has recently
114 been prioritized by the IMERG development team—specifically, to provide uncertainty estimates

115 at IMERG's native 30-minute, 0.1° resolution and at the time of creating IMERG data files
116 (Huffman et al., 2019; Jackson Tan, personal communication, 30 December 2020).

117 A more limited number of studies have sought to develop so-called error models that attempt
118 to characterize the uncertainty associated with any particular SMP product, generally expressed in
119 the form of a probability distribution of "true precipitation" (e.g., Sarachi et al., 2015; Wright et
120 al., 2017). Error model development is challenging due in part to the mixed discrete-continuous
121 nature of intermittent precipitation, an issue that becomes increasingly important to address as
122 SMP products advance to higher spatial and temporal resolutions. Some error models just ignore
123 intermittency altogether to focus on hit biases and random errors (e.g., Sarachi et al., 2015; Tian
124 et al., 2013), while others have attempted to address it (e.g., Gebremichael et al., 2011; Hossain &
125 Anagnostou, 2006; Maggioni et al., 2014a), but arguably at the expense of relatively complicated
126 formulations and limited flexibility (Wright et al., 2017). An alternative approach has been also
127 proposed to characterize uncertainty as an integral part of SMP retrieval algorithms, and to
128 subsequently yield probabilistic precipitation estimates (Kirstetter et al., 2018).

129 Regardless of the specific error model formulation, the availability of ground reference data
130 to train these models has posed a fundamental limitation, since reference measurements are lacking
131 precisely in the locations (i.e., data-sparse regions) that could benefit most from spaceborne remote
132 sensing (e.g., Gebregiorgis & Hossain, 2014). It is thus highly desired to explore universal
133 uncertainty quantification approaches that can perform anywhere, even in the total absence of local
134 or regional ground reference observations.

135 In this study, we explore the idea that the Dual-frequency Precipitation Radar (DPR) on board
136 the Global Precipitation Measurement (GPM) core observatory—the most accurate spaceborne
137 precipitation measurement instrument to date—can be utilized in place of ground reference data.
138 If valid, this facilitates the development of worldwide native-resolution error estimates of IMERG.
139 Recent studies have explored the potential for DPR as an alternative reference to evaluate PMW-
140 only precipitation estimates (e.g., Adhikari et al., 2019; You et al., 2020), and merged precipitation
141 products (Khan et al., 2018). This study advances that concept to propose a prototype uncertainty
142 quantification framework for IMERG. We use two DPR derived products and co-located IMERG
143 estimates to train a parsimonious mixed discrete-continuous error model. These DPR-trained error
144 models are evaluated against alternative models trained on ground reference observations over the
145 contiguous United States (CONUS). The error model can also incorporate additional predictors.
146 We examine whether a NASA reanalysis dataset can further constrain IMERG uncertainties. As
147 far as we are aware, this is the first study to explore the feasibility of a globally-applicable
148 prototype framework for quantification at the IMERG native resolution, though we leave global
149 validation and several other important details to future work.

150 The datasets used in this study are described in Section 2. The data resampling and matching
151 algorithm, the error model, and evaluation metrics are introduced in Section 3. Section 4 presents
152 the results; discussion follows in Section 5. A summary and conclusions are provided in Section
153 6.

154 **2 Data**

155 We selected CONUS as the study area (Figure 1) for two reasons: firstly, it is covered by a
156 high-quality, high-resolution NASA-sanctioned ground reference precipitation product that allows
157 us to validate the proposed approach; secondly, its large geographic extent and climatic diversity
158 allows a relatively comprehensive assessment of the approach's robustness. The study period is
159 June 2014 to April 2019 (~ 5years). No attempt is made to address seasonally-varying uncertainty,
160 nor to discriminate by precipitation phase. Prior studies have argued that the former may not be
161 critical (Maggioni et al., 2014b; Wright et al., 2017), while the latter certainly is.

162 2.1 IMERG

163 IMERG merges all available PMW estimates with IR observations to produce 30-minute, 0.1°
164 gridded precipitation estimates over the entire globe (Huffman et al., 2020; Tan et al., 2016). Three
165 variants—Early (hereafter IMERG-E), Late and Final—address different user requirements for
166 latency and accuracy. This study focuses on version 06B IMERG-E (Huffman et al., 2019), which
167 is arguably the most useful for realtime applications due to its short latency (4 hours for IMERG-
168 E, compared to 12 hours and 2 months for Late and Final, respectively) but features the largest
169 errors due to the more limited availability of short-latency satellite and ground observations.

170 While the IMERG processing algorithm consists of many elements beyond the scope of this
171 study, it is worth mentioning that it uses observations from the DPR and GPM Microwave Imager
172 (GMI) on board the GPM core observatory. Microwave radiances from all partner constellation
173 PMW sensors are calibrated to GMI for a bias-corrected, consistent radiometric dataset before
174 retrieving precipitation rates (Hou et al., 2014). Then, the combined DPR and GMI data product

175 from the GPM Combined Radar–Radiometer algorithm (CORRA; Grecu et al., 2016) contributes
176 to IMERG in terms of its derived hydrometeor profiles and surface precipitation. The former is
177 used to construct a-priori hydrometeor databases in the Goddard profiling algorithm (GPROF;
178 Kummerow et al., 2015; Randel et al., 2020) to convert the calibrated PMW radiances into
179 precipitation, while the latter is used to calibrate those PMW-only precipitation estimates on a
180 rolling 45-day basis over ocean (the calibration is based on the Global Precipitation Climatology
181 Project data over land; Huffman et al., 2019). We mention this because it constitutes a potential
182 objection to the usage of DPR (and, as the reader will see, GMI) as the reference for uncertainty
183 estimation due to a possible lack of independence between IMERG and those instruments. This
184 issue is discussed further in Section 5.1.

185 2.2 Ground Reference: GV-MRMS

186 The Ground Validation Multi-radar/Multi-Sensor (GV-MRMS; Kirstetter et al., 2012, 2018)
187 dataset is derived from the MRMS system that combines the polarimetric WSR-88D CONUS radar
188 network with rain gauges and other auxiliary information to generate high-resolution quantitative
189 precipitation estimates (QPE) over CONUS (Zhang et al., 2016). GV-MRMS QPE has been used
190 as a ground reference for evaluation of various satellite precipitation products (Gebregiorgis et al.,
191 2018; Kirstetter et al., 2012, 2014, 2020; O & Kirstetter, 2018). In this study, we use the Level-3
192 regrided GV-MRMS QPE product, which was created specifically to support GPM ground
193 validation (Kirstetter et al., 2020). This product includes a 30-minute, 0.01° gauge-corrected

194 precipitation rate (GCP) as well as a radar quality index (RQI) which ranges from 0 to 100, with
195 100 representing the best quality.

196 2.3 DPR-based Reference Datasets

197 We consider two recent (version 06) GPM Level-2 DPR products as potential alternatives to
198 a ground-based reference: 2ADPR and 2BCMB. Both provide high-resolution (approximately 5
199 km DPR footprint diameter at nadir) precipitation estimates on an instantaneous field of view basis
200 between 65°N and 65°S. 2ADPR is derived based on Ku (13.6 GHz) and Ka (35.5 GHz) band DPR
201 measurements and it uses dual-frequency observations to infer precipitation phase and reconstruct
202 three-dimensional hydrometeor and precipitation fields (Iguchi, 2020; Iguchi et al., 2018). This
203 study uses the 2ADPR data field “precipRateESurface”, which is extrapolated from the lowest
204 clutter-free DPR bin to estimate surface precipitation rate (Petracca et al., 2018). 2BCMB, on the
205 other hand, combines DPR reflectivities and GMI radiances using the CORRA algorithm to offer
206 the highest-quality precipitation estimates from spaceborne sensors (Hou et al., 2014). We use the
207 2BCMB data field “surfPrecipTotRate” in the following analysis.

208 Both 2ADPR and 2BCMB data fields are obtained from normal scans (i.e., the widest swath
209 scans from DPR; Iguchi et al., 2018) to maximize sample size. While 2BCMB and 2ADPR present
210 different error structures (Gatlin et al., 2020), post-launch evaluations showed that DPR and GMI
211 can detect precipitation rates down to 0.1 mm h⁻¹ (e.g., Adhikari et al., 2019; Hamada & Takayabu,
212 2016). This precipitation rate was thus selected as the rain/no-rain detection threshold in this study
213 for all datasets.

214 2.4 Additional Predictors: MERRA-2

215 We also examine the potential to further constrain the uncertainty estimates by incorporating
216 additional predictors such as the total precipitable water vapor (TQV), topmost soil layer's ground
217 wetness index ($GWET_{TOP}$), and 2-m air temperature (T2M) from NASA's MERRA-2 reanalysis
218 product (Gelaro et al., 2017). To match with the above datasets, this study uses 0.5° (latitude)
219 $\times 0.625^\circ$ (longitude), hourly MERRA-2 outputs. $GWET_{TOP}$ is a dimensionless relative saturation
220 index for the upper 5 cm of soil. Based on previous studies showing that soil moisture changes can
221 enhance satellite precipitation estimation (e.g., Brocca et al., 2014; Crow et al., 2011), we also
222 derive a variable we call $GWETD_{TOP}$, which is the difference between the current and preceding
223 value of $GWET_{TOP}$. Negative values of $GWETD_{TOP}$ correspond to soil evaporation, while positive
224 values indicate precipitation occurrence. We transform all the negative $GWETD_{TOP}$ values to zero
225 before including it as a predictor in the uncertainty framework.

226 It should be emphasized here that our goal was not to identify the best possible additional
227 predictors, but rather to simply illustrate that such predictors could be utilized to constrain IMERG
228 uncertainty estimates. This issue is discussed further in Section 5.3.

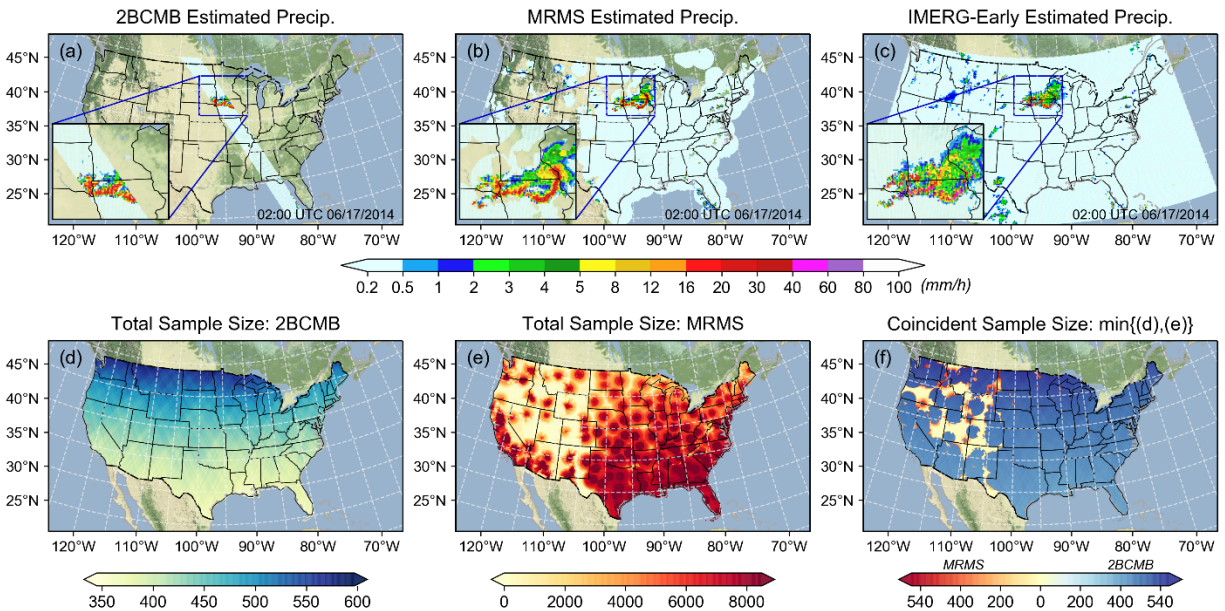
229

230 **3 Methodology**

231 3.1 Matching and Preprocessing of Multiple Datasets

232 Following the approach of Khan et al. (2018), IMERG-E, GV-MRMS, DPR, and MERRA-2
233 data are matched in space and time to a consistent 0.1° 30-minute grid. GV-MRMS is upscaled by
234 averaging all grid cells in a 10×10 window, provided that the RQI for at least 90% of these pixels

235 is 100. The two DPR derived products are regridded by averaging all the DPR footprint scale (~5
 236 km) estimates falling within a 0.1° grid cell, and then matched into the nearest 30-minute IMERG
 237 observation interval. MERRA-2 is mapped into the IMERG grid using nearest neighbor
 238 interpolation, and also matched to the nearest 30-minute IMERG observation interval. Figure 1
 239 (upper panels) shows an example of the regridded coincident precipitation estimates from 2BCMB,
 240 GV-MRMS and IMERG-E.



241
 242 **Figure 1.** Coincident precipitation estimates from regridded (a) 2BCMB (2ADPR is similar; see Supplemental
 243 Figure S1), (b) GV-MRMS, and (c) IMERG-E for 02:00–03:00 UTC 17 June 2014, with the maps for the total
 244 sample size of (d) 2BCMB (also 2ADPR), (e) GV-MRMS, and (f) the coincident sample size—the minimum
 245 from (d) and (e)—within $0.1^\circ \times 0.1^\circ$ boxes during the study period.

246 The sample size of DPR products generally decreases from north to south due to the inclined
 247 orbit of GPM (Figure 1d), while GV-MRMS data is limited in western CONUS because of radar
 248 beam blockage (Figure 1e). The coincident data sample size thus depends on location and is
 249 generally less than 600 in each 0.1° grid cell (Figure 1f). To ensure a sufficiently large sample

250 size, error models are trained and validated by pooling all coincident 0.1° data samples within
 251 $1^\circ \times 1^\circ$ spatial windows. In some parts of western CONUS this pooling is insufficient; in windows
 252 where the sample size is less than 5,000, we further pool data from the adjacent four windows in
 253 the east–west and north–south directions.

254 3.2 CSGD-based Uncertainty Quantification Framework

255 The uncertainty quantification framework selected in this study follows the censored shifted
 256 gamma distribution (CSGD) method developed by Scheuerer & Hamill (2015) for postprocessing
 257 ensemble numerical precipitation forecasts. It was adapted by Wright et al., (2017) to characterize
 258 the uncertainty for daily-scale satellite precipitation estimates. The CSGD is able to simultaneously
 259 depict precipitation occurrence and magnitude by introducing a “shift” parameter δ ($\delta < 0$) into the
 260 conventional two-parameter gamma distribution $F_{\mu,\sigma}$ (parameterized here by its mean μ and
 261 standard deviation σ , rather than shape and scale/rate parameters). The cumulative distribution
 262 function (CDF) of the CSGD is left-censored at zero:

$$F_{\mu,\sigma,\delta}(x) = \begin{cases} F_{\mu,\sigma}(x - \delta), & \text{for } x \geq 0 \\ 0, & \text{for } x < 0 \end{cases} \quad (1)$$

263 where x is precipitation rate (mm h^{-1}). The vertical intercept $F_{\mu,\sigma,\delta}(0)$ is one minus the probability
 264 of precipitation (POP), and the CDF to the right of zero represents the nonexceedance probabilities
 265 associated with nonzero precipitation rates.

266 The CSGD-based error model consists of two main pieces: 1.) a “climatological CSGD” with
 267 parameters μ, σ, δ [i.e., Eqn. (1)]; and 2.) a regression system that comprises the error model. Once
 268 trained, this regression system can produce an estimated “conditional” CSGD with parameters $\mu(t)$,

269 $\sigma(t)$, and $\delta(t)$ that represents the possible true precipitation rate and POP conditioned on an IMERG
 270 retrieval at time t (and other optional predictors). This regression system can capture both
 271 conditional bias and heteroscedasticity, as well as the discrete-continuous nature of precipitation
 272 and associated errors. The most basic regression system lets $\mu(t)$ increase linearly with IMERG
 273 magnitude $P_I(t)$, and all models used here assume that $\sigma(t)$ is proportional to the square root of $\mu(t)$
 274 (see Scheuerer & Hamill, 2015). We will refer to this most basic variant as the “linear model”:

$$\mu(t) = \mu \left[\alpha_2 + \alpha_3 \frac{P_I(t)}{\bar{P}_I} \right] \quad (2)$$

$$\sigma(t) = \alpha_4 \sigma \sqrt{\frac{\mu(t)}{\mu}} \quad (3)$$

$$\delta(t) = \delta \quad (4)$$

275 where \bar{P}_I denotes the climatological IMERG mean.

276 The linearity assumption can be further relaxed to account for nonlinear conditional bias. This
 277 version (hereafter “nonlinear model”) replaces Eqn. (2) with:

$$\mu(t) = \frac{\mu}{\alpha_1} \log 1p \left\{ \exp m1(\alpha_1) \left[\alpha_2 + \alpha_3 \frac{P_I(t)}{\bar{P}_I} \right] \right\} \quad (5)$$

278 where $\log 1p(x) = \log(1+x)$, and $\exp m1(x) = \exp(x) - 1$.

279 Both the linear and nonlinear models can also accommodate extra time-varying predictors or
 280 covariates $C(t)$, potentially further constraining (i.e., narrowing) uncertainty estimates. To this end,
 281 Eqns. (2) and (5) can be replaced with:

$$\mu(t) = \mu \left[\alpha_2 + \alpha_3 \frac{P_I(t)}{\bar{P}_I} + \alpha_5 \frac{C(t)}{\bar{C}} \right] \quad (6)$$

$$\mu(t) = \frac{\mu}{\alpha_1} \log 1 p \left\{ \text{expm1}(\alpha_1) \left[\alpha_2 + \alpha_3 \frac{P_I(t)}{\bar{P}_I} + \alpha_5 \frac{C(t)}{\bar{C}} \right] \right\}, \quad (7)$$

282 respectively, where \bar{C} is the climatological mean of the covariate. While multiple covariates can be
 283 used simultaneously (not depicted in Eqns. 6–7; Scheuerer & Hamill, 2015 and Wright et al., 2017),
 284 this study only considers covariates individually.

285 All of the above regression coefficients (α_1 – α_5) as well as the three CSGD parameters are
 286 optimally estimated using the techniques detailed in Scheuerer & Hamill (2015), which minimize
 287 the continuous ranked probability score (CRPS) between empirical and theoretical CDFs.

288 3.3 Error Model Training and Validation

289 2ADPR and 2BCMB are first compared against coincident GV-MRMS observations over
 290 CONUS. This comparison considers the ability to correctly detect precipitation occurrence and to
 291 estimate precipitation rates of hit cases. To evaluate precipitation occurrence, we create
 292 contingency tables showing the numbers and rates of hits, misses, false alarms, and correct non-
 293 detects (Wilks, 2019) using 0.1 mm h⁻¹ as the detection threshold (see Section 2.3). Precipitation
 294 rates for hits are then assessed for every 1°×1° spatial window in terms of three evaluation metrics:
 295 relative bias (RB), root mean squared error (RMSE), and Pearson’s correlation coefficient (CC),
 296 which have been widely used in previous studies (e.g., Tan et al., 2018; Khan et al., 2018).

297 The regridded coincident datasets are randomly divided with 80% of observations used for
 298 CSGD-based error model training and 20% for validating model performance. A range of error

299 model complexities are explored: linear models [Eqns. (1)–(4)], nonlinear models [Eqns. (1), (3)–
 300 (5)], linear models with a single covariate [Eqns. (1), (3), (4), (6)], and nonlinear models with a
 301 single covariate [Eqns. (1), (3), (4), (7)]. All the error models are trained using both the selected
 302 DPR data and GV-MRMS, while the latter are used as performance benchmarks to evaluate if the
 303 proposed DPR-based model appears reasonable.

304 DPR- and GV-MRMS-trained error models are then applied to the validation dataset, and
 305 their conditional CSGD estimates of reference precipitation are evaluated against GV-MRMS
 306 observations from that dataset using both deterministic and probabilistic metrics. To examine if
 307 the model can effectively characterize the central tendency of IMERG error, we compare the
 308 conditional CSGD median with GV-MRMS using mean absolute error (MAE):

$$\text{MAE} = \frac{1}{n} \sum_{t=1}^n |y_t - o_t| \quad (8)$$

309 where y_t is either the CSGD median or IMERG, o_t is the coincident GV-MRMS observation at
 310 time t , and n is the number of (y_t, o_t) pairs.

311 Similar to other deterministic evaluation metrics (e.g., RB, RMSE, CC), MAE is insufficient
 312 for fully characterizing the predicted (probabilistic) distributions from CSGD error models. CRPS,
 313 on the other hand, measures the dispersion of these distributions around a GV-MRMS observation.
 314 CRPS thus offers a probabilistic performance measure of the error models:

$$\text{CRPS}(F_{\mu(t),\sigma(t),\delta(t)}, o_t) = \int_{-\infty}^{\infty} [F_{\mu(t),\sigma(t),\delta(t)}(x) - \mathbf{I}(o_t \leq x)]^2 dx \quad (9)$$

315 where $F_{\mu(t),\sigma(t),\delta(t)}$ denotes the CDF of the conditional CSGD model at time t , and $\mathbf{I}(\cdot)$ is a step

316 function that takes the value of 1 if $x \geq o_t$ (i.e., GV-MRMS observation at time t) and 0 elsewhere.
317 Low CRPS indicates that the predicted CSGD's density is concentrated relatively close to the
318 reference, while high CRPS implies either a very "wide" distribution or one that is heavily biased.
319 Note that CRPS is mathematically identical to MAE for deterministic—as opposed to
320 probabilistic—predictions.

321 Heteroscedasticity in IMERG errors means that we should not simply compare or combine
322 CRPS values across various locations, since, like MAE or RMSE, CRPS will tend to be larger for
323 heavier precipitation regimes. This has three implications for our model validation. First of all, we
324 apply "reduction CRPS" (RCRPS; Trinh et al., 2013) for comparing model performance across
325 different locations (i.e., $1^\circ \times 1^\circ$ boxes). It is normalized by the standard deviation of GV-MRMS
326 observations at that location (denoted as σ_M) and thus is dimensionless:

$$\text{RCRPS} = \frac{\text{CRPS}}{\sigma_M} \quad (10)$$

327 Second, the validation dataset is then grouped into four categories: hits, misses, false alarms,
328 and correct non-detects, by comparing the coincident IMERG and GV-MRMS data (using the
329 same 0.1 mm h^{-1} threshold). CRPS is then calculated for each group to evaluate model performance
330 under different cases. In addition, the calculated CRPSs of hit cases are further grouped by the
331 magnitude of IMERG, to investigate the magnitude-dependent performance of the uncertainty
332 estimates from different error models.

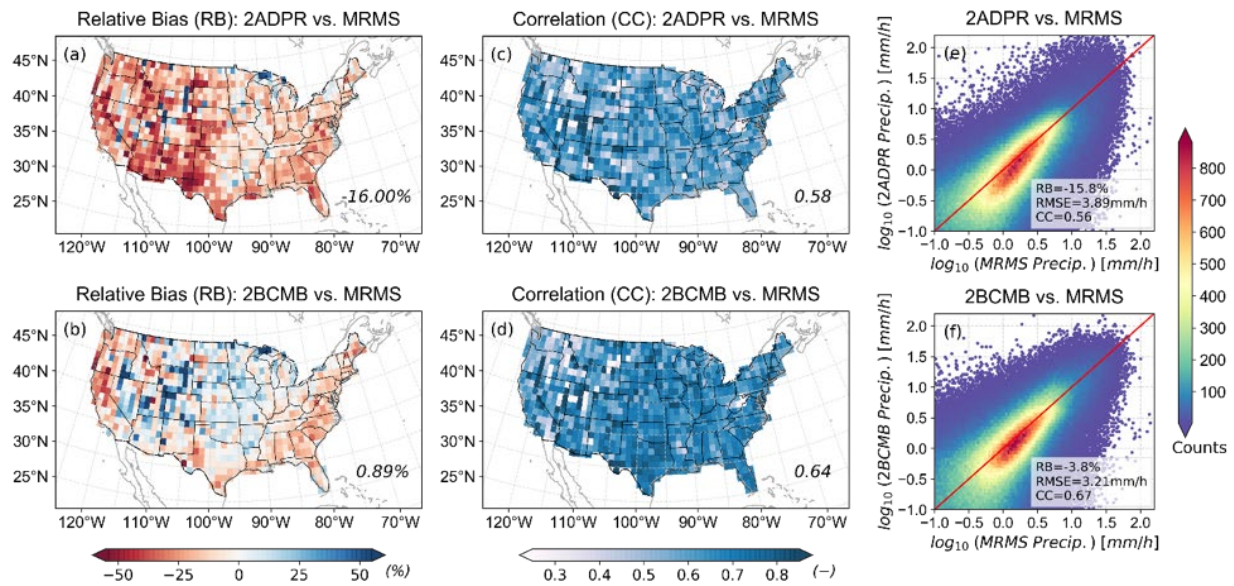
333 Finally, we further examine the performance of the error models' probabilistic estimates of

334 precipitation events given a number of thresholds using reliability diagrams (see Wilks, 2019 for
 335 details). Considering GV-MRMS observation o_t and the CDF of CSGD error model $F_{\mu(t),\sigma(t),\delta(t)}$ at
 336 time t , the observed and predicted probability that an “event” occurred can be defined:

$$X_{e,t} = \begin{cases} 1, & \text{for } o_t > TH \\ 0, & \text{for } o_t \leq TH \end{cases} \quad (11)$$

$$Y_{e,t} = 1 - F_{\mu(t),\sigma(t),\delta(t)}(TH) \quad (12)$$

337 where TH is the threshold (mm h^{-1}). $X_{e,t}$ denotes the observed probability of threshold exceedance
 338 (either 0 or 1), while $Y_{e,t}$ is the predicted probability of threshold exceedance (between 0 and 1)
 339 from the error model. Following previous studies (e.g., Clark & Slater, 2006; Ghazvinian et al.,
 340 2020), we sort and group all predicted probabilities $Y_{e,t}$ (e.g., $t=1, 2, \dots, N$ for validation dataset)
 341 into ten equally-sized bins (0–10%, 10%–20%, ..., 90%–100%). For each group, both the average
 342 predicted probability and the average observed probability are calculated. In a reliability diagram,
 343 a perfect prediction model would yield results that fall along the 1:1 line. For example, when $Y_{e,t}$
 344 = 0.90, we expect the event to occur 90% of the time in reality. All coincident samples across
 345 CONUS are pooled for this analysis.



346

347 **Figure 2.** The spatial maps of (a-b) relative bias, (c-d) correlation coefficient, and (e-f) density scatterplots by
 348 comparing the coincident precipitation estimates from 2ADPR and 2BCMB versus GV-MRMS during the study
 349 period. Only precipitation estimates greater than 0.1 mm h^{-1} are considered. Inset values in (a)-(d) are the mean
 350 across all grid boxes ($1^\circ \times 1^\circ$) over CONUS.

351

352 4 Results

353 4.1 DPR Products as Reference Precipitation

354 Figure 2 shows CONUS-wide evaluation “hits only” results of DPR derived products against
 355 coincident GV-MRMS observations. 2ADPR underestimates precipitation almost everywhere,
 356 particularly in the western parts of the country leading to a CONUS-wide average underestimation
 357 of 16% (Figure 2a). 2BCMB, on the other hand, varies geographically with overestimation (e.g.,
 358 the Rockies and Great Plains) and modest underestimation (e.g., the West and East Coasts) leading
 359 to a CONUS-wide average within 1% of GV-MRMS (Figure 2b). Moreover, 2BCMB is better
 360 correlated with GV-MRMS observations over most of CONUS (Figures 2c-d). Scatterplots and
 361 three summary statistics (RB, RMSE, and CC) again indicate that 2BCMB generally outperforms

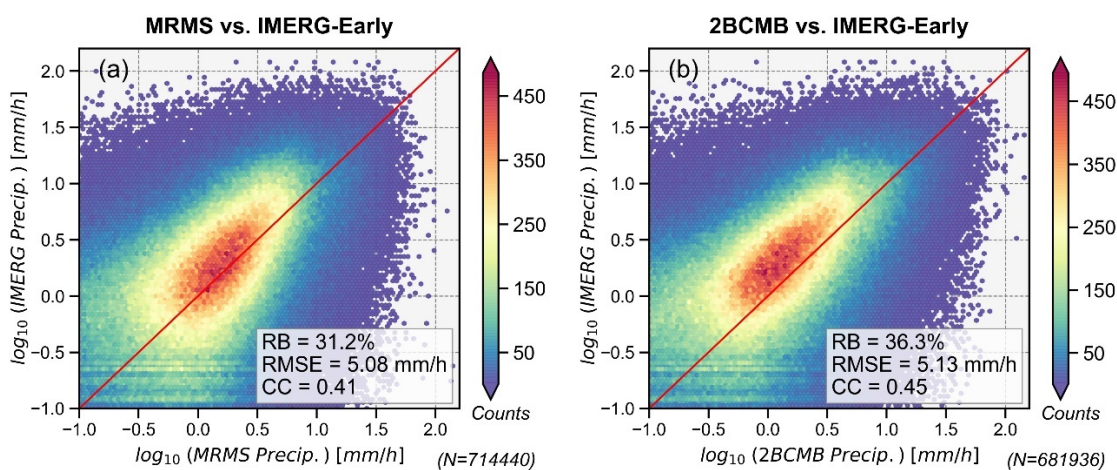
362 2ADPR (Figures 2e–f). 2ADPR, however, shows somewhat better detection skills—lower
 363 numbers of false alarms and missed precipitation (Table 1). From Table 1, however, it can be seen
 364 that hits are more common than false alarms and missed precipitation. They are also probably more
 365 important in the context of applications, which tend to focus on medium-to-heavy rainfall in which
 366 hits are prevalent. Prioritizing “hit-relevant” performance such as bias and correlation, we have
 367 elected to focus on 2BCMB for the remainder of this study. This issue deserves further attention,
 368 however, as the relative performance of 2ADPR and 2BCMB can be expected to vary
 369 geographically, seasonally, and with precipitation microphysics (Skofronick-Jackson et al., 2017;
 370 Skofronick-Jackson et al., 2018).

371 **Table 1.** The contingency tables of 2ADPR and 2BCMB, benchmarking against the ground reference GV-
 372 MRMS. For each pair of estimates, hits (top left), false alarms (top right), misses (bottom left), and correct non-
 373 detects (bottom right) are shown. The total paired data sample size over CONUS is 20,986,107.

	$P_{GV-MRMS} \geq 0.1 \text{ mm h}^{-1}$	$P_{GV-MRMS} < 0.1 \text{ mm h}^{-1}$
$P_{2ADPR} \geq 0.1 \text{ mm h}^{-1}$	931,165 (4.4%)	52,187 (0.2%)
$P_{2ADPR} < 0.1 \text{ mm h}^{-1}$	44,407 (0.2%)	19,958,348 (95.1%)
$P_{2BCMB} \geq 0.1 \text{ mm h}^{-1}$	833,803 (4.0%)	324,859 (1.5%)
$P_{2BCMB} < 0.1 \text{ mm h}^{-1}$	141,769 (0.7%)	19,685,676 (93.8%)

374 In addition to the absolute precipitation estimation performance, another key consideration is
 375 the need for approximate (if not strict) independence from the SMP product being evaluated, if
 376 DPR derived products are to be used as alternative references. Khan et al. (2018) and You et al.,
 377 (2020) argue that the independence need can be approximately met as numerous processing steps
 378 and assumptions stand between the DPR/GMI observations and their manifestation within IMERG
 379 (as highlighted in Section 2.1). Nonetheless, we examined this by comparing the accuracy of

380 IMERG (for hits only) relative to both 2BCMB and GV-MRMS (Figure 3). The RBs between
 381 IMERG and the two reference datasets are similar (31% in the case of GV-MRMS, and 36% for
 382 2BCMB; while visual inspection shows different conditional bias features). RMSEs are very
 383 similar (5.08 versus 5.13 mm h⁻¹), while Pearson correlation CC with 2BCMB is slightly higher
 384 (0.45) than with GV-MRMS (0.41). Contingency tables corresponding to Figure 3 are shown in
 385 Supplemental Table S1 and reveal similar detection skills of IMERG relative to 2BCMB and GV-
 386 MRMS. Taken together, these results suggest that there is indeed approximate independence
 387 between IMERG and 2BCMB, confirming the latter's potential to evaluate the former. This issue
 388 is discussed further in Section 5.1.



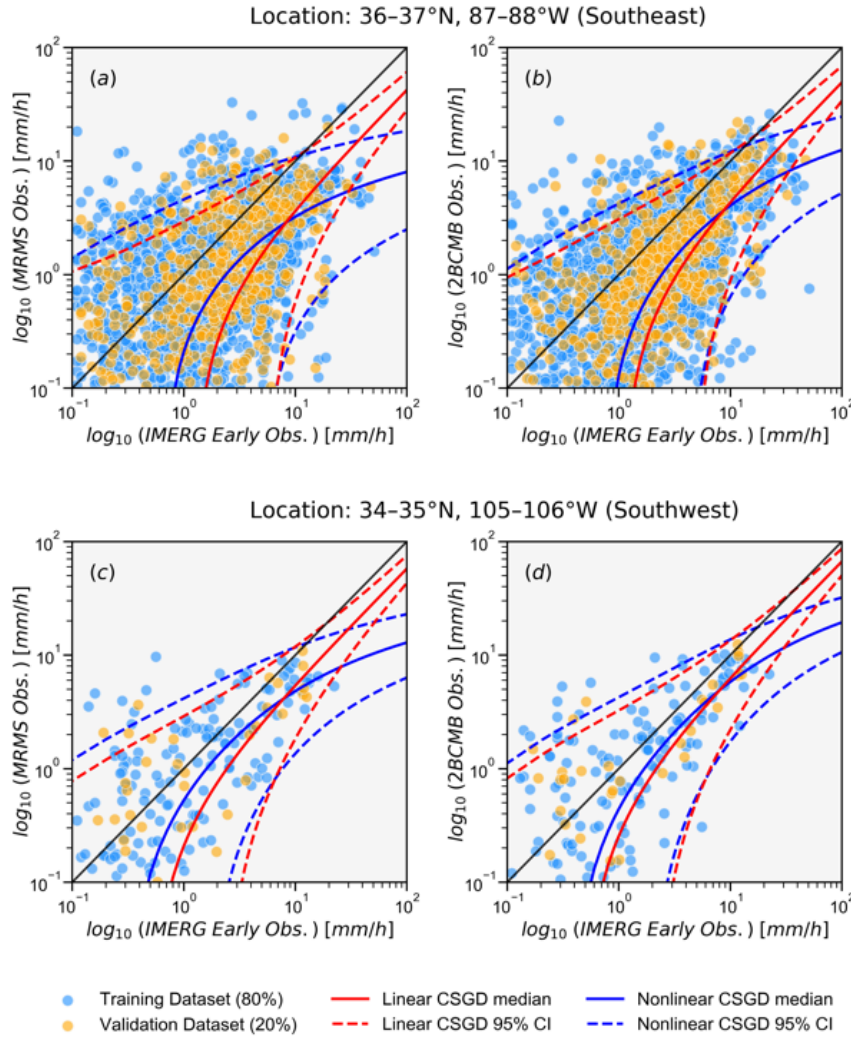
389
 390 **Figure 3.** Density scatterplots of coincident precipitation estimates from GV-MRMS and 2BCMB versus
 391 IMERG. Only precipitation estimates greater than 0.1 mm h⁻¹ are considered, including all the data samples over
 392 the CONUS during the study period.

393 Climatological CSGDs fitted to GV-MRMS and 2BCMB share similar spatial patterns of μ
 394 and POP (Supplemental Figures S2a–d; σ and δ were also investigated but are not shown). 2BCMB
 395 tends to slightly underestimate μ and POP relative to GV-MRMS, likely reflecting its imperfect

396 detection and quantification. Fitted CDFs for climatological CSGDs are illustrated for a $1^\circ \times 1^\circ$ box
397 in the state of Tennessee in the Southeastern CONUS and a $1^\circ \times 1^\circ$ box in New Mexico in the
398 Southwest (Figures S2e–f), which are randomly selected to represent the locations characterized
399 by different climates. Although these CSGDs closely match the empirical CDFs over the more
400 humid Southeastern box, 2BCMB exhibits a higher probability of zero precipitation and relatively
401 large differences from GV-MRMS for light precipitation rates less than 1 mm h^{-1} (Figure S2e). In
402 the drier Southwest, a small negative bias in estimated POP is evident (Figure S2f), consistent with
403 previous studies and related to the CRPS minimization scheme (Ghazvinian et al., 2020).

404 4.2 CSGD Error Model Visual Inspection and Deterministic Performance

405 Linear and nonlinear versions of the CSGD error models trained by GV-MRMS and 2BCMB
406 are further compared over the $1^\circ \times 1^\circ$ boxes in the Southeast and Southwest CONUS (Figure 4; see
407 Figure S3 for identical results plotted on linear rather than log-log scales). For these selected boxes
408 and other locations in the CONUS, IMERG is prone to overestimate precipitation at half-an-hour
409 scale, particularly at higher precipitation rates. This is consistent with previous regional studies
410 (e.g., Tan et al., 2017; Moazami and Najafi, 2021) and CONUS-wide analysis (Gebregiorgis et al.,
411 2018).



412

413 **Figure 4.** Linear (red lines) and nonlinear (blue lines) conditional CSGD models for (a, b) the Southeast $1^\circ \times 1^\circ$
 414 box and (c, d) Southwest $1^\circ \times 1^\circ$ box, trained and compared against GV-MRMS (left panels) and 2BCMB (right
 415 panels). See Figure S2 for identical results, but plotted on linear scales.

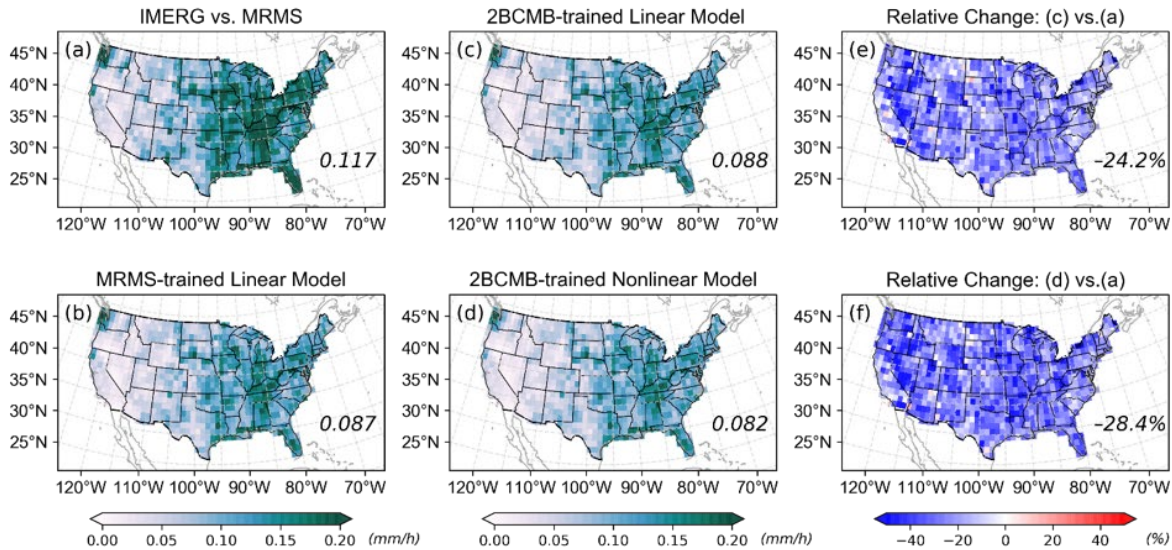
416

The nonlinear models in Figure 4 perform better than linear models for capturing the
 417 conditional bias that is evident at high precipitation rates (e.g., $>10 \text{ mm h}^{-1}$). Visual inspection
 418 suggests that the 2BCMB-trained models have similar features to the GV-MRMS-trained models,
 419 though the nonlinear versions show slightly weaker systematic bias and a wider uncertainty bound.

420

Both GV-MRMS- and 2BCMB-trained CSGD models provide reasonable fits to the validation

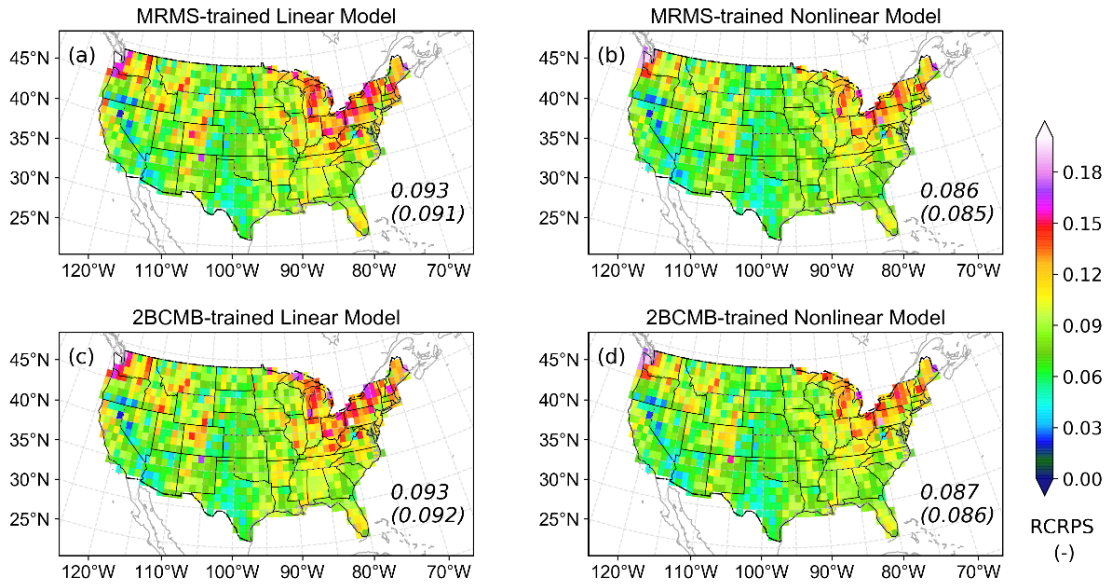
421 dataset, showing the robustness of this uncertainty quantification framework. The sample size of
 422 coincident data for the more arid southwestern box (Figures 4c–d) is limited due to lower POP,
 423 while IMERG systematic bias is somewhat lower than in the Southeast (Figures 4a–b). These
 424 results highlight the relative flexibility of this CSGD-based uncertainty quantification method
 425 under very different climatic conditions.



426
 427 **Figure 5.** MAE calculated relative to GV-MRMS: (a) IMERG, and the median predicted by (b) GV-MRMS-
 428 trained linear model, (c) 2BCMB-trained linear model, and (d) 2BCMB-trained nonlinear model. Relative
 429 percentage change of MAE relative to IMERG results in (a): (e) 2BCMB-trained linear model, and (f)
 430 2BCMB-trained nonlinear model. All the results are calculated by validation data samples, and inset values
 431 are the means of all $1^\circ \times 1^\circ$ boxes in the CONUS.

432 The central tendency (i.e., means or medians) predicted by the CSGD error model represent
 433 the reducible IMERG error (i.e., bias; see Wright et al., 2017). We compare the CSGD medians
 434 predicted by the GV-MRMS- and 2BCMB-trained error models over CONUS against GV-MRMS
 435 observations using MAE (Figures 5a–d). The 2BCMB-trained linear (nonlinear) models can
 436 isolate bias in IMERG—reducing MAE by 24.2% (28.4%) on average (Figures 5e–f). The GV-

437 MRMS-trained model performs similarly (see Figure 5d for the linear model; nonlinear model not
 438 shown). There is no obvious change in MAE incorporating GWTD_{TOP} (inset statistics in Figure 6)
 439 or other MERRA-2 predictors (results not shown), indicating that these variables have limited roles
 440 in explaining IMERG systematic error.

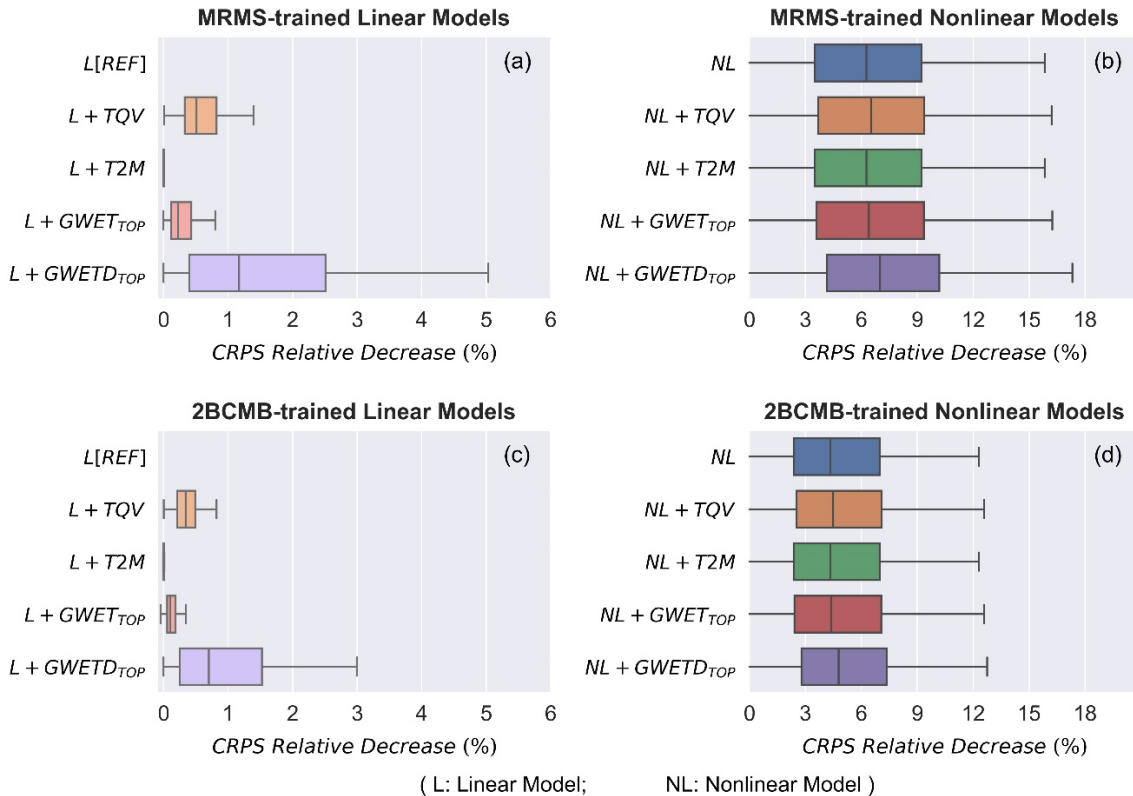


441
 442 **Figure 6.** The comparison of mean RCRPS maps for (a) GV-MRMS-trained linear model, (b) GV-MRMS-
 443 trained nonlinear model; (c) 2BCMB-trained linear model, and (d) 2BCMB-trained nonlinear model. Inset
 444 values are the means of all $1^\circ \times 1^\circ$ boxes in the CONUS, and the results for nonlinear models with GWTD_{TOP}
 445 are in parentheses.

446 4.3 CONUS-wide Probabilistic Evaluation

447 Figure 6 presents the mean RCRPS maps for different error models over CONUS. The results
 448 show somewhat lower CONUS-averaged RCRPS for the nonlinear GV-MRMS- and 2BCMB-
 449 trained models (0.086 and 0.087, respectively) compared to the linear models (0.093 for both the
 450 GV-MRMS- and 2BCMB-based models). This highlights both the potential of 2BCMB as a
 451 reference product and confirms the superiority of the nonlinear model. Interestingly, the areas with
 452 highest RCRPS—e.g., Northeast CONUS, the Rockies, the Great Lakes states, and the Pacific

453 Northwest—still show relatively high RCRPS values after considering nonlinear bias. This reflects
 454 region-dependent IMERG uncertainties, likely associated with relatively high precipitation totals
 455 combined with “complicating factors” such as orography, lake-effect snow, and high fractions of
 456 annual precipitation falling as snow.



457
 458 **Figure 7.** Boxplots of the percentage decrease in CRPS relative to the linear model with no predictors for (a-
 459 b) GV-MRMS-trained models, and (c-d) 2BCMB-trained models with various model complexities and
 460 predictors. The results are calculated based on training data samples, including all the $1^\circ \times 1^\circ$ boxes in the
 461 CONUS. The covariates TQV, T2M, $GWET_{TOP}$ represent the total precipitable water vapor, 2-m air
 462 temperature and topmost soil layer’s ground wetness index from MERRA-2 respectively, and $GWETD_{TOP}$ is
 463 the ground wetness change indicator that is derived from $GWET_{TOP}$.

4.4 Model Complexity and Conditional Performance

464 We compared CONUS-wide performance improvements for a range of GV-MRMS- and
 465 2BCMB-based error models with varied model complexities, measured by the percentage decrease
 466

467 of CRPS relative to the linear model without any covariate (Figure 7). Consistent with Figure 4,
468 nonlinearity is the most critical model feature for constraining uncertainty (i.e., improving CRPS).
469 Moreover, the improvement gained via the nonlinear formulation tends to be larger for the GV-
470 MRMS-based model than for the 2BCMB-based model (a mean of 6% vs. 4%, respectively),
471 consistent with the larger conditional bias “detected” by GV-MRMS as shown in Figures 4 and
472 S2. Figure 7 also shows that the most informative covariate we evaluated is GWTD_{TOP}, which can
473 provide modest improvements (generally 0.5-1.5% reduction in CRPS; ranging as high as 5% in
474 some locations) to both the linear and nonlinear models. On average, the other covariates—TQV,
475 T2M, GWTD_{TOP}—provide more limited benefits. Therefore, only GWTD_{TOP} is shown elsewhere
476 in this study.

477 We further group the validation dataset and corresponding model predictions into four cases:
478 hits, misses, false alarms and correct non-detects. Table 2 summarizes CONUS-wide mean CRPS
479 values of the four groups. Since the number of instances of the groups differ widely, we also show
480 an overall “weighted mean” for each model. In general, the 2BCMB-based model shows similar
481 performance as GV-MRMS-trained model in characterizing both the overall uncertainty and the
482 errors associated with these four cases. The results highlight that the role of model nonlinearity
483 and GWTD_{TOP} may vary among different cases. The nonlinear model shows improved
484 performance in both hits and correct non-detects cases, but performs worse than the linear model
485 for misses and false alarms. Because the correct non-detects and hits dominate in the coincident
486 samples (accounting for 92.6% and 3.4% of the validation dataset, respectively), the weighted

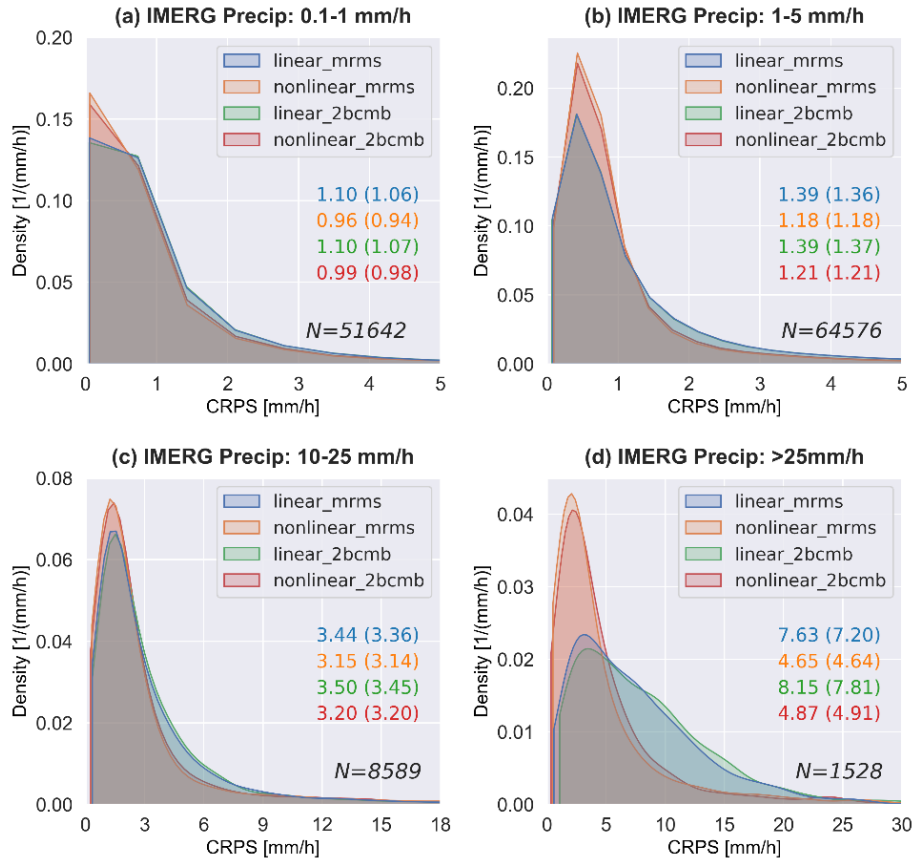
487 mean CRPS of the nonlinear model outperforms that of the linear version.

488 **Table 2.** The CONUS-wide mean CRPS for different cases: hits (3.4% of validation data), misses (2.0%), false
 489 alarms (2.0%) and correct non-detects (92.6%), and their weighted mean according to the percentage of different
 490 cases in validation dataset.

Cases ¹	Mean CRPS for different model complexities (mm h ⁻¹)			
	GV-MRMS-trained Linear Model		GV-MRMS-trained Nonlinear Model	
	No Covariate	With GWTD _{TOP}	No Covariate	With GWTD _{TOP}
Hits	1.484	1.449	1.282	1.275
Correct Non-detects	0.0009	0.0013	0.0003	0.0007
Misses	0.913	0.889	0.924	0.903
False Alarms	0.132	0.131	0.219	0.214
Weighted Mean	0.072	0.071	0.067	0.066
	2BCMB-trained Linear Model		2BCMB-trained Nonlinear Model	
	No Covariate	With GWTD _{TOP}	No Covariate	With GWTD _{TOP}
	Hits	1.497	1.470	1.330
Correct Non-detects	0.0004	0.0007	0.0001	0.0003
Misses	0.922	0.904	0.931	0.916
False Alarms	0.133	0.132	0.190	0.186
Weighted Mean	0.072	0.071	0.067	0.067

491 ¹: The four cases are divided based on GV-MRMS and the coincident IMERG observations. The percentages
 492 of each case are similar to those in Table S1, but only the validation dataset is considered here.

493 At the same time, GWTD_{TOP} improves the uncertainty estimates for hits and misses, and the
 494 latter particularly. GWTD_{TOP} can indicate precipitation occurrence using changes in land surface
 495 wetness conditions, and it thus helps in quantifying the “missed” precipitation that is difficult to
 496 address in most SMP products, even with gauge corrections (Li et al., 2015; Tian et al., 2009).
 497 However, the inclusion of GWTD_{TOP} also increases CRPS in cases of correct non-detects.



498

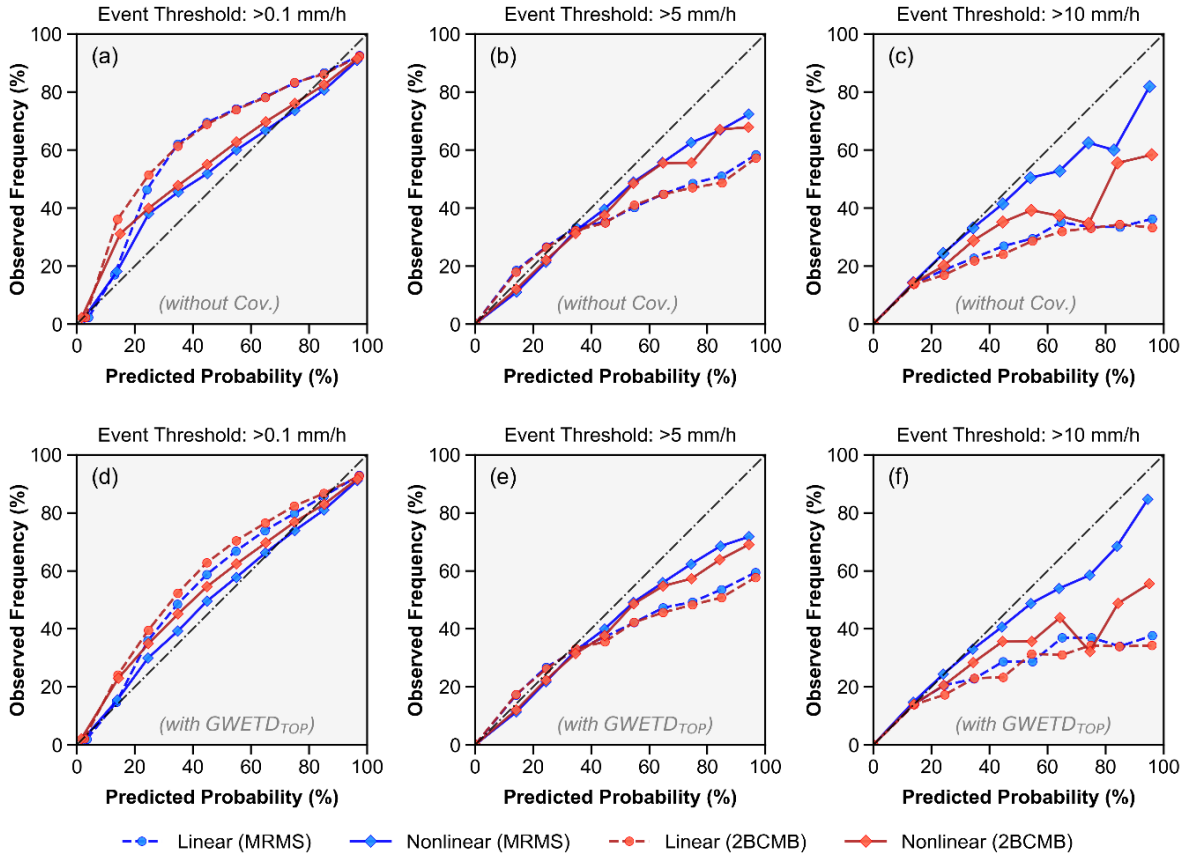
499 **Figure 8.** Distributions of CRPS for GV-MRMS- and 2BCMB-trained models for different intervals of
500 IMERG precipitation rates (validation data samples of “hits” only; N is sample size). Inset values are the
501 mean CRPS [mm h⁻¹] for the different models. Values inside (outside) the parentheses include (don’t include)
502 GWTD_{TOP} as a predictor.

503 To better characterize the magnitude-dependent performance of the uncertainty estimates for
504 hit cases, we consider 0.1, 1, 5, 10, and 25 mm h⁻¹ thresholds, which roughly correspond to the
505 0.97, 0.99, 0.995, and 0.998 quantiles of IMERG climatology. Figure 8 shows kernel-based density
506 functions of CRPS for IMERG data between these thresholds. For IMERG-detected precipitation
507 events, the nonlinear model outperforms the linear model, as the distributions of CRPS of the
508 former are more concentrated towards zero and thus have a smaller mean. For larger IMERG
509 estimates, differences become more apparent and the nonlinear models yield smaller CRPS scores
510 than the linear models (Figures. 8c–d). This is unsurprising, since IMERG shows substantial

511 nonlinear conditional bias at high precipitation rates (e.g., Figure 4). This analysis also shows that
512 the 2BCMB-trained models perform similarly to the GV-MRMS-trained model at different
513 precipitation intensities, showing slight degradation for very heavy precipitation ($>25 \text{ mm h}^{-1}$),
514 likely attributable to attenuation. The benefits of adding GWTD_{TOP} is not visually obvious in these
515 CRPS-based analyses; it does offer very modest benefits, however, particularly in the linear
516 models at higher precipitation rates (inset statistics in Figure 8).

517 Reliability diagrams for all the error models with thresholds of 0.1 mm h^{-1} , 5 mm h^{-1} , and 10
518 mm h^{-1} are compared in Figure 9. The results clearly shows that the nonlinear model always offers
519 more reliable estimates than the linear model (i.e., it always falls closer to the 1:1 line). The
520 2BCMB-based nonlinear model presents similar skill to the GV-MRMS-trained model, except for
521 events larger than 10 mm h^{-1} . The model reliability varies at different event thresholds. For
522 precipitation occurrence (i.e., 0.1 mm h^{-1}), all error models tend to be consistently above the
523 diagonal, particularly at low-medium forecast probability categories. This feature indicates that
524 the observed frequency in each category exceeds the model estimated frequency (i.e., a “dry bias”;
525 Wilks, 2019). This is similar to the findings of an earlier study on CSGD models (Ghazvinian et
526 al., 2020) that relate this dry bias to the underestimation of POP by climatological CSGDs (which
527 can be seen in Figure. S2f). This dry bias is reduced by incorporating GWTD_{TOP} , which is
528 unsurprising since it serves as an “indicator” of precipitation occurrence. For heavy events, on the
529 other hand, all error models fall below the diagonal at high forecast probability categories,
530 indicating the model tends to overestimate occurrence frequency. As discussed in Scheuerer et al.

531 (2017), however, the uncertainty in observed frequency increases at higher precipitation rates due
 532 to limited sample sizes.



533
 534 **Figure 9.** Reliability diagrams for GV-MRMS- and 2BCMB-trained models with various event thresholds.
 535 The upper panels are for models without covariates, and lower panels are for models with $GWETD_{TOP}$.

536
 537 **5 Discussion**

538 **5.1 DPR Data as Reference**

539 Our findings point to the promise of DPR products—and particularly 2BCMB—to serve as a
 540 reference in the proposed global IMERG uncertainty estimation framework. It must be recognized,
 541 however, that while 2BCMB generally outperforms 2ADPR over CONUS (Figure 2; though not
 542 in terms of precipitation detection; see Table 1), this conclusion may not hold in other places

543 around the globe. The rejection of 2ADPR as a reference here is not inconsistent with Khan et al.,
544 (2018), who showed that conditional biases in IMERG and 2ADPR are similar.

545 Despite the similar error modeling results between 2BCMB- and GV-MRMS-trained error
546 models, the two references differ in important ways: 2BCMB estimates instantaneous precipitation
547 rate, while GV-MRMS offers precipitation estimates aggregated into 30-minute intervals. This
548 scale mismatch inevitably will introduce additional uncertainties, which are likely to manifest in
549 the form of random errors both in precipitation occurrence and magnitude. This seems unlikely to
550 influence systematic errors. It should be noted that 2BCMB underestimates high precipitation
551 rates, probably due to attenuation of radar signals. This likely explains the somewhat poor
552 performance of the 2BCMB-based error models at high precipitation rates, relative to performance
553 at lower intensities.

554 As mentioned in Sections 2.1 and 4.1, an objection can be raised to the use of DPR-derived
555 datasets as reference for IMERG or other GPM precipitation data products, owing to the (generally
556 indirect) inclusion of DPR (and GMI, in the case of 2BCMB) in those products and thereby the
557 potential for lack of independence between them and the DPR-based reference. Those results in
558 Section 4.1 and the arguments of Khan et al. (2018) and You et al. (2020) suggest that this
559 objection should not be overly concerning. The most direct contribution from DPR and GMI
560 combined data in IMERG algorithm is the 45-day probability matching intercalibration of PMW-
561 only precipitation retrievals, before the morphing and PMW-IR merging procedures that derive
562 the ultimate gridded IMERG estimates (Huffman et al., 2020). The actual difference in IMERG

563 estimates before and after this intercalibration is found to typically be less than 10% (Jackson Tan,
564 personal communication, 7 April 2021). Nonetheless, recent work by Kirstetter et al. (2020) shows
565 that systematic biases such as those associated with precipitation typology display similar features
566 across Level-2 and Level-3 GPM products (i.e., QPE from DPR, GPROF-GMI, and IMERG),
567 suggesting that uncertainty can propagate from DPR-based precipitation estimates into the SMP
568 product.

569 5.2 CSGD-based Error Model

570 This study demonstrates that the CSGD error model can reasonably characterize IMERG
571 uncertainty over CONUS. Consistent with previous studies (Hartke et al., 2020; Wright et al.,
572 2017), model fitting was relatively robust to small sample sizes (Figure 5). This property is crucial
573 if the framework is to be expanded to the entire globe, as GPM DPR sampling frequency decreases
574 at lower latitudes (Figure 1d, and Figure 1 in You et al., 2020).

575 The inclusion of additional predictors into the model provides a way of improving uncertainty
576 estimates. As demonstrated in this study, incorporating $GWTD_{TOP}$ derived from the MERRA-2
577 reanalysis product modestly improved the model's performance in characterizing precipitation
578 occurrence (Table 2, and Figure 9). Expectation of greater gains using MERRA-2 is unwarranted
579 given its coarse temporal and particularly spatial resolution. It isn't clear that other satellite-based
580 products could be much help here—consider, for example, that remotely-sensed soil moisture data
581 likely lack the combination of global coverage and short latency needed to inform near real-time
582 IMERG uncertainty estimates. High-resolution global-scale numerical weather forecasts such as

583 those from NASA’s Goddard Earth Observing System Forward Processing products (GEOS-FP;
584 Molod et al., 2012), on the other hand, seem to offer potential as they are available on a consistent
585 global basis in realtime. Another direction which is being explored in separate work is using simple
586 metrics derived from the IMERG precipitation fields themselves as predictors in the error model.

587 Finally, while we explored several deterministic and probabilistic performance measures in
588 this study, it is doubtful that we have fully explored all relevant aspects of model skill. Future
589 global validation efforts will continue exploring this topic using more candidate evaluation metrics
590 (e.g., Massari & Maggioni, 2020; Wilks, 2019) and in varied environmental settings.

591 5.3 IMERG Uncertainty Beyond the DPR Swath

592 This study’s central premise—that DPR measurements on board the GPM core observatory
593 can serve as an alternative reference for estimating IMERG uncertainty—carries a key limitation:
594 since spatial and temporal coincidence between IMERG and DPR is needed to train the error model,
595 this can only occur within the DPR swath. Of course, DPR and GMI are co-located on the GPM
596 core observatory. The result is that the uncertainty estimates presented here primarily reflect the
597 relationships between DPR and GMI-influenced IMERG. Because GMI is the most accurate PMW
598 precipitation radiometer currently in space (Skofronick-Jackson et al., 2018), our analyses
599 probably provide the “best scenario” (i.e., lowest uncertainty); the real uncertainty associated with
600 IMERG estimates that are dominated by other PMW or IR sensors or morphing is likely greater
601 (e.g., Tan et al., 2016, and Li et al., 2020; also see Figure S3) than our models would predict.

602 To overcome this limitation, more work is needed to examine how DPR-based uncertainty
603 estimates can be “inflated” to better reflect the properties of other PMW and IR sensors as well as
604 IMERG’s morphing scheme. The work of You et al. (2020)—who compared 2ADPR precipitation
605 estimates against those of different PMW sensors within GPROF—provides a possible blueprint
606 for addressing this.

607

608 **6 Summary and Conclusions**

609 This study proposes a prototype uncertainty quantification framework for satellite
610 precipitation products, in which GPM DPR-derived observations are used in place of ground-based
611 measurements. Though we focus our study on the IMERG-Early dataset at its native 30-minute,
612 0.1° resolution over CONUS, the quasi-global availability of DPR measurements allows this
613 framework to be applied across the globe to any satellite precipitation dataset whose
614 spatiotemporal resolution is similar to that of IMERG, such as CMORPH and PERSIANN.
615 Uncertainty is modeled using a flexible and parsimonious three-parameter censored shifted gamma
616 distribution (CSGD) error model which can characterize the probability of precipitation as well as
617 intensity-dependent systematic bias and the potential range of random error. Uncertainty estimates
618 from the CSGD error model trained on the 2BCMB reference are compared against high-quality
619 ground observations from the GV-MRMS dataset, as well as uncertainties inferred from GV-
620 MRMS-based versions of the error model. We believe this is the first study to generate IMERG
621 uncertainty estimates using this general approach.

622 Our CONUS-wide assessment suggests that the combined (DPR and GMI) product 2BCMB
623 outperforms 2ADPR (which uses DPR exclusively) in terms of precipitation intensity statistics.
624 2ADPR has somewhat better detection properties, however. Due to substantial intensity-dependent
625 error behaviors in IMERG, the rejection of 2ADPR as a reference by Khan et al. (2018), and the
626 supposition that better uncertainty estimates during precipitating periods would be preferable to
627 better estimates of detection uncertainty, we focused our error modeling analysis on the 2BCMB
628 product.

629 Multiple CSGD-based IMERG error models of varying complexity were trained using both
630 GV-MRMS and 2BCMB. We find that the precipitation climatology characterized by GV-MRMS-
631 and 2BCMB-based models yield similar properties and comparable performance throughout
632 CONUS, though the 2BCMB-based model has slightly lower mean and POP values, likely
633 attributable to its imperfect detection skill. 2BCMB-based model performance also suffers at high
634 precipitation rates compared with GV-MRMS-based models. Evaluation using CRPS indicates
635 that IMERG uncertainty, for both models, is relatively high at the Northeast CONUS, the Rockies,
636 and the Pacific Northwest, where a number of “complicating factors” such as orography, lake-
637 effect snow, as well as high fractions of annual precipitation falling as snow may complicate
638 IMERG errors.

639 Relatively weak error model performance can be ameliorated by incorporating additional
640 predictors to further constrain uncertainty estimates. We illustrate this by incorporating predictors
641 from NASA’s MERRA-2 reanalyses, including a derived variable representing positive temporal
642 deviations in near-surface soil moisture that can be associated with precipitation occurrence and

643 that improves uncertainty estimates, albeit modestly. Higher-resolution numerical weather
644 predictions—particularly short-range high-resolution global forecasts—could be potentially useful
645 for informing uncertainty estimates for near-realtime versions of IMERG. In addition, variables
646 derived from IMERG’s ancillary data or the spatial structure of the IMERG fields themselves offer
647 further promise to constrain IMERG uncertainty.

648 Despite the promising performance of this uncertainty framework over CONUS, its flexibility
649 and robustness in other parts of the globe remain untested. The accuracy of IMERG as well as the
650 relative performance of the 2ADPR and 2BCMB products are influenced by climate, land surface
651 conditions, and atmospheric and precipitation properties (e.g., Khan et al., 2018; Tang et al., 2016).
652 DPR’s sampling frequency also varies with latitude due to its inclined orbit. Future work will focus
653 on validating uncertainty estimates in other locations and conditions.

654 Notwithstanding these remaining challenges, the IMERG uncertainty estimates provided by
655 this error modeling framework can benefit end-user applications (Kirschbaum et al., 2017). As
656 illustrated in a recent study, the incorporation of CSGD-based satellite precipitation uncertainty
657 can improve regional landslide hazard nowcasting, even when a CSGD error model is trained by
658 very limited data (Hartke et al., 2020). It should be noted that the maximum benefits of the IMERG
659 error modeling framework only can be achieved when regional and global environmental modeling
660 systems and workflows are adapted to “ingest” such uncertainty information. Proof-of-concept
661 efforts in that direction are equally important as further validation of our uncertainty estimation
662 approach.

663 **Acknowledgements:**

664 Z. Li's and D.B. Wright's contributions were funded by NASA Precipitation Measurement
665 Mission Grant 80NSSC19K0951. S. H. Hartke was supported by the NASA Earth and Space
666 Science Fellowship Program (Grant 80NSSC18K1321). IMERG, 2ADPR and 2BCMB were
667 downloaded from the NASA GES DISC website <https://disc.gsfc.nasa.gov/>. The authors would
668 like to thank GPM Ground Validation team for preparing the regridded GV-MRMS dataset, which
669 is available at <https://pmm-gv.gsfc.nasa.gov/>.

670

671

672

673 **REFERENCES:**

674 Adhikari, A., Liu, C., & Hayden, L. (2019). Uncertainties of GPM Microwave Imager Precipitation Estimates
675 Related to Precipitation System Size and Intensity. *Journal of Hydrometeorology*, 20(9), 1907–1923.

676 <https://doi.org/10.1175/JHM-D-19-0038.1>

677 AghaKouchak, A., Mehran, A., Norouzi, H., & Behrangi, A. (2012). Systematic and random error components
678 in satellite precipitation data sets: SYSTEMATIC AND RANDOM ERROR COMPONENTS.

679 *Geophysical Research Letters*, 39(9), n/a-n/a. <https://doi.org/10.1029/2012GL051592>

680 Beck, H. E., Pan, M., Roy, T., Weedon, G. P., Pappenberger, F., van Dijk, A. I. J. M., et al. (2019). Daily
681 evaluation of 26 precipitation datasets using Stage-IV gauge-radar data for the CONUS. *Hydrology*

682 *and Earth System Sciences*, 23(1), 207–224. <https://doi.org/10.5194/hess-23-207-2019>

- 683 Behrangi, A., & Wen, Y. (2017). On the Spatial and Temporal Sampling Errors of Remotely Sensed
684 Precipitation Products. *Remote Sensing*, 9(11), 1127. <https://doi.org/10.3390/rs9111127>
- 685 Brocca, L., Ciabatta, L., Massari, C., Moramarco, T., Hahn, S., Hasenauer, S., et al. (2014). Soil as a natural
686 rain gauge: Estimating global rainfall from satellite soil moisture data: Using the soil as a natural
687 raingauge. *Journal of Geophysical Research: Atmospheres*, 119(9), 5128–5141.
688 <https://doi.org/10.1002/2014JD021489>
- 689 Clark, M. P., & Slater, A. G. (2006). Probabilistic Quantitative Precipitation Estimation in Complex Terrain.
690 *Journal of Hydrometeorology*, 7(1), 3–22. <https://doi.org/10.1175/JHM474.1>
- 691 Crow, W. T., van den Berg, M. J., Huffman, G. J., & Pellarin, T. (2011). Correcting rainfall using satellite-
692 based surface soil moisture retrievals: The Soil Moisture Analysis Rainfall Tool (SMART): SOIL
693 MOISTURE ANALYSIS RAINFALL TOOL. *Water Resources Research*, 47(8).
694 <https://doi.org/10.1029/2011WR010576>
- 695 Ebert, E. E., Janowiak, J. E., & Kidd, C. (2007). Comparison of Near-Real-Time Precipitation Estimates from
696 Satellite Observations and Numerical Models. *Bulletin of the American Meteorological Society*, 88(1),
697 47–64. <https://doi.org/10.1175/BAMS-88-1-47>
- 698 Foufoula-Georgiou, E., Guilloteau, C., Nguyen, P., Aghakouchak, A., Hsu, K.-L., Busalacchi, A., et al. (2020).
699 Advancing Precipitation Estimation, Prediction, and Impact Studies. *Bulletin of the American*
700 *Meteorological Society*, 101(9), E1584–E1592. <https://doi.org/10.1175/BAMS-D-20-0014.1>
- 701 Gatlin, P. N., Petersen, W. A., Pippitt, J. L., Berendes, T. A., Wolff, D. B., & Tokay, A. (2020). The GPM
702 Validation Network and Evaluation of Satellite-Based Retrievals of the Rain Drop Size Distribution.
703 *Atmosphere*, 11(9), 1010. <https://doi.org/10.3390/atmos11091010>

- 704 Gebregiorgis, A., & Hossain, F. (2014). Making Satellite Precipitation Data Work for the Developing World.
705 *IEEE Geoscience and Remote Sensing Magazine*, 2(2), 24–36.
706 <https://doi.org/10.1109/MGRS.2014.2317561>
- 707 Gebregiorgis, Abebe S., Kirstetter, P., Hong, Y. E., Gourley, J. J., Huffman, G. J., Petersen, W. A., et al. (2018).
708 To What Extent is the Day 1 GPM IMERG Satellite Precipitation Estimate Improved as Compared to
709 TRMM TMPA-RT? *Journal of Geophysical Research: Atmospheres*, 123(3), 1694–1707.
710 <https://doi.org/10.1002/2017JD027606>
- 711 Gebregiorgis, Abebe Sine, Kirstetter, P.-E., Hong, Y. E., Carr, N. J., Gourley, J. J., Petersen, W., & Zheng, Y.
712 (2017). Understanding Overland Multisensor Satellite Precipitation Error in TMPA-RT Products.
713 *Journal of Hydrometeorology*, 18(2), 285–306. <https://doi.org/10.1175/JHM-D-15-0207.1>
- 714 Gebremichael, M., Liao, G.-Y., & Yan, J. (2011). Nonparametric error model for a high resolution satellite
715 rainfall product: NONPARAMETRIC ERROR MODEL. *Water Resources Research*, 47(7).
716 <https://doi.org/10.1029/2010WR009667>
- 717 Gelaro, R., McCarty, W., Suárez, M. J., Todling, R., Molod, A., Takacs, L., et al. (2017). The Modern-Era
718 Retrospective Analysis for Research and Applications, Version 2 (MERRA-2). *Journal of Climate*,
719 30(14), 5419–5454. <https://doi.org/10.1175/JCLI-D-16-0758.1>
- 720 Ghazvinian, M., Zhang, Y., & Seo, D.-J. (2020). A Nonhomogeneous Regression-Based Statistical
721 Postprocessing Scheme for Generating Probabilistic Quantitative Precipitation Forecast. *Journal of*
722 *Hydrometeorology*, 21(10), 2275–2291. <https://doi.org/10.1175/JHM-D-20-0019.1>

- 723 Greu, M., Olson, W. S., Munchak, S. J., Ringerud, S., Liao, L., Haddad, Z., et al. (2016). The GPM Combined
724 Algorithm. *Journal of Atmospheric and Oceanic Technology*, *33*(10), 2225–2245.
725 <https://doi.org/10.1175/JTECH-D-16-0019.1>
- 726 Guilloteau, C., Foufoula-Georgiou, E., & Kummerow, C. D. (2017). Global Multiscale Evaluation of Satellite
727 Passive Microwave Retrieval of Precipitation during the TRMM and GPM Eras: Effective Resolution
728 and Regional Diagnostics for Future Algorithm Development. *Journal of Hydrometeorology*, *18*(11),
729 3051–3070. <https://doi.org/10.1175/JHM-D-17-0087.1>
- 730 Hamada, A., & Takayabu, Y. N. (2016). Improvements in Detection of Light Precipitation with the Global
731 Precipitation Measurement Dual-Frequency Precipitation Radar (GPM DPR). *Journal of Atmospheric
732 and Oceanic Technology*, *33*(4), 653–667. <https://doi.org/10.1175/JTECH-D-15-0097.1>
- 733 Hartke, S. H., Wright, D. B., Kirschbaum, D. B., Stanley, T. A., & Li, Z. (2020). Incorporation of Satellite
734 Precipitation Uncertainty in a Landslide Hazard Nowcasting System. *Journal of Hydrometeorology*,
735 *21*(8), 1741–1759. <https://doi.org/10.1175/JHM-D-19-0295.1>
- 736 Hossain, F., & Anagnostou, E. N. (2006). A two-dimensional satellite rainfall error model. *IEEE Transactions
737 on Geoscience and Remote Sensing*, *44*(6), 1511–1522. <https://doi.org/10.1109/TGRS.2005.863866>
- 738 Hou, A. Y., Kakar, R. K., Neeck, S., Azarbarzin, A. A., Kummerow, C. D., Kojima, M., et al. (2014). The
739 Global Precipitation Measurement Mission. *Bulletin of the American Meteorological Society*, *95*(5),
740 701–722. <https://doi.org/10.1175/BAMS-D-13-00164.1>
- 741 Huffman, G. J., Bolvin, D. T., Nelkin, E. J., Wolff, D. B., Adler, R. F., Gu, G., et al. (2007). The TRMM
742 Multisatellite Precipitation Analysis (TMPA): Quasi-Global, Multiyear, Combined-Sensor

- 743 Precipitation Estimates at Fine Scales. *Journal of Hydrometeorology*, 8(1), 38–55.
- 744 <https://doi.org/10.1175/JHM560.1>
- 745 Huffman, G. J., Bolvin, D. T., Braithwaite, D., Hsu, K., Joyce, R., Kidd, C., et al. (2019, March 13). Algorithm
- 746 Theoretical Basis Document (ATBD) Version 06, NASA Global Precipitation Measurement (GPM)
- 747 Integrated Multi-satellitE Retrievals for GPM (IMERG).
- 748 Huffman, G. J., Bolvin, D. T., Braithwaite, D., Hsu, K.-L., Joyce, R. J., Kidd, C., et al. (2020). Integrated
- 749 Multi-satellite Retrievals for the Global Precipitation Measurement (GPM) Mission (IMERG). In V.
- 750 Levizzani, C. Kidd, D. B. Kirschbaum, C. D. Kummerow, K. Nakamura, & F. J. Turk (Eds.), *Satellite*
- 751 *Precipitation Measurement* (Vol. 67, pp. 343–353). Cham: Springer International Publishing.
- 752 https://doi.org/10.1007/978-3-030-24568-9_19
- 753 Iguchi, T. (2020). Dual-Frequency Precipitation Radar (DPR) on the Global Precipitation Measurement (GPM)
- 754 Mission’s Core Observatory. In V. Levizzani, C. Kidd, D. B. Kirschbaum, C. D. Kummerow, K.
- 755 Nakamura, & F. J. Turk (Eds.), *Satellite Precipitation Measurement* (Vol. 67, pp. 183–192). Cham:
- 756 Springer International Publishing. https://doi.org/10.1007/978-3-030-24568-9_11
- 757 Iguchi, T., Seto, S., Meneghini, R., Yoshida, N., Awaka, J., Le, M., et al. (2018, October). GPM/DPR Level-2
- 758 Algorithm Theoretical Basis Document.
- 759 Joyce, R. J., & Xie, P. (2011). Kalman Filter–Based CMORPH. *Journal of Hydrometeorology*, 12(6), 1547–
- 760 1563. <https://doi.org/10.1175/JHM-D-11-022.1>
- 761 Joyce, R. J., Janowiak, J. E., Arkin, P. A., & Xie, P. (2004). CMORPH: A Method that Produces Global
- 762 Precipitation Estimates from Passive Microwave and Infrared Data at High Spatial and Temporal

- 763 Resolution. *Journal of Hydrometeorology*, 5(3), 487–503. <https://doi.org/10.1175/1525->
764 7541(2004)005<0487:CAMTPG>2.0.CO;2
- 765 Khan, S., Maggioni, V., & Kirstetter, P.-E. (2018). Investigating the Potential of Using Satellite-Based
766 Precipitation Radars as Reference for Evaluating Multisatellite Merged Products. *Journal of*
767 *Geophysical Research: Atmospheres*, 123(16), 8646–8660. <https://doi.org/10.1029/2018JD028584>
- 768 Kidd, Chris, & Maggioni, V. (2020). *Quantifying errors and uncertainties in satellite precipitation estimates*
769 (other). display. <https://doi.org/10.5194/egusphere-egu2020-5857>
- 770 Kidd, Chris, Becker, A., Huffman, G. J., Muller, C. L., Joe, P., Skofronick-Jackson, G., & Kirschbaum, D. B.
771 (2017). So, How Much of the Earth’s Surface Is Covered by Rain Gauges? *Bulletin of the American*
772 *Meteorological Society*, 98(1), 69–78. <https://doi.org/10.1175/BAMS-D-14-00283.1>
- 773 Kidd, Christopher, Takayabu, Y. N., Skofronick-Jackson, G. M., Huffman, G. J., Braun, S. A., Kubota, T., &
774 Turk, F. J. (2020). The Global Precipitation Measurement (GPM) Mission. In V. Levizzani, C. Kidd,
775 D. B. Kirschbaum, C. D. Kummerow, K. Nakamura, & F. J. Turk (Eds.), *Satellite Precipitation*
776 *Measurement* (Vol. 67, pp. 3–23). Cham: Springer International Publishing.
777 https://doi.org/10.1007/978-3-030-24568-9_1
- 778 Kirschbaum, D. B., Huffman, G. J., Adler, R. F., Braun, S., Garrett, K., Jones, E., et al. (2017). NASA’s
779 Remotely Sensed Precipitation: A Reservoir for Applications Users. *Bulletin of the American*
780 *Meteorological Society*, 98(6), 1169–1184. <https://doi.org/10.1175/BAMS-D-15-00296.1>
- 781 Kirstetter, P.-E., Hong, Y., Gourley, J. J., Chen, S., Flamig, Z., Zhang, J., et al. (2012). Toward a Framework for
782 Systematic Error Modeling of Spaceborne Precipitation Radar with NOAA/NSSL Ground Radar–

- 783 Based National Mosaic QPE. *Journal of Hydrometeorology*, 13(4), 1285–1300.
- 784 <https://doi.org/10.1175/JHM-D-11-0139.1>
- 785 Kirstetter, P.-E., Hong, Y., Gourley, J. J., Cao, Q., Schwaller, M., & Petersen, W. (2014). Research Framework
786 to Bridge from the Global Precipitation Measurement Mission Core Satellite to the Constellation
787 Sensors Using Ground-Radar-Based National Mosaic QPE. In V. Lakshmi, D. Alsdorf, M. Anderson,
788 S. Biancamaria, M. Cosh, J. Entin, et al. (Eds.), *Geophysical Monograph Series* (pp. 61–79).
789 Hoboken, NJ: John Wiley & Sons, Inc. <https://doi.org/10.1002/9781118872086.ch4>
- 790 Kirstetter, P.-E., Petersen, W. A., & Gourley, J. J. (2018). GPM Ground Validation Multi-Radar/Multi-Sensor
791 (MRMS) Precipitation Reanalysis for Satellite Validation Product. NASA Global Hydrology Resource
792 Center DAAC, Huntsville, Alabama, U.S.A. Retrieved from
793 <https://ghrc.nsstc.nasa.gov/hydro/details/gpmmrms>
- 794 Kirstetter, P.-E., Karbalae, N., Hsu, K., & Hong, Y. (2018). Probabilistic precipitation rate estimates with
795 space-based infrared sensors. *Quarterly Journal of the Royal Meteorological Society*, 144, 191–205.
796 <https://doi.org/10.1002/qj.3243>
- 797 Kirstetter, P.-E., Petersen, W. A., Kummerow, C. D., & Wolff, D. B. (2020). Integrated Multi-satellite
798 Evaluation for the Global Precipitation Measurement: Impact of Precipitation Types on Spaceborne
799 Precipitation Estimation. In V. Levizzani, C. Kidd, D. B. Kirschbaum, C. D. Kummerow, K.
800 Nakamura, & F. J. Turk (Eds.), *Satellite Precipitation Measurement* (Vol. 69, pp. 583–608). Cham:
801 Springer International Publishing. https://doi.org/10.1007/978-3-030-35798-6_7
- 802 Kummerow, C. D., Randel, D. L., Kulie, M., Wang, N.-Y., Ferraro, R., Joseph Munchak, S., & Petkovic, V.
803 (2015). The Evolution of the Goddard Profiling Algorithm to a Fully Parametric Scheme. *Journal of*
LI ET AL.

- 804 *Atmospheric and Oceanic Technology*, 32(12), 2265–2280. <https://doi.org/10.1175/JTECH-D-15->
805 0039.1
- 806 Lettenmaier, D. P., Alsdorf, D., Dozier, J., Huffman, G. J., Pan, M., & Wood, E. F. (2015). Inroads of remote
807 sensing into hydrologic science during the WRR era: REMOTE SENSING. *Water Resources*
808 *Research*, 51(9), 7309–7342. <https://doi.org/10.1002/2015WR017616>
- 809 Li, Z., Yang, D., & Hong, Y. (2013). Multi-scale evaluation of high-resolution multi-sensor blended global
810 precipitation products over the Yangtze River. *Journal of Hydrology*, 500, 157–169.
811 <https://doi.org/10.1016/j.jhydrol.2013.07.023>
- 812 Li, Z., Yang, D., Gao, B., Jiao, Y., Hong, Y., & Xu, T. (2015). Multiscale Hydrologic Applications of the Latest
813 Satellite Precipitation Products in the Yangtze River Basin using a Distributed Hydrologic Model.
814 *Journal of Hydrometeorology*, 16(1), 407–426. <https://doi.org/10.1175/JHM-D-14-0105.1>
- 815 Li, Z., Wright, D. B., Zhang, S. Q., Kirschbaum, D. B., & Hartke, S. H. (2020). Object-Based Comparison of
816 Data-Driven and Physics-Driven Satellite Estimates of Extreme Rainfall. *Journal of*
817 *Hydrometeorology*, 21(12), 2759–2776. <https://doi.org/10.1175/JHM-D-20-0041.1>
- 818 Maggioni, V., Sapiano, M. R. P., Adler, R. F., Tian, Y., & Huffman, G. J. (2014a). An Error Model for
819 Uncertainty Quantification in High-Time-Resolution Precipitation Products. *Journal of*
820 *Hydrometeorology*, 15(3), 1274–1292. <https://doi.org/10.1175/JHM-D-13-0112.1>
- 821 Maggioni, V., Sapiano, M. R. P., Adler, R. F., Tian, Y., & Huffman, G. J. (2014b). An Error Model for
822 Uncertainty Quantification in High-Time-Resolution Precipitation Products. *Journal of*
823 *Hydrometeorology*, 15(3), 1274–1292. <https://doi.org/10.1175/JHM-D-13-0112.1>

- 824 Maggioni, V., Meyers, P. C., & Robinson, M. D. (2016). A Review of Merged High-Resolution Satellite
825 Precipitation Product Accuracy during the Tropical Rainfall Measuring Mission (TRMM) Era. *Journal*
826 *of Hydrometeorology*, 17(4), 1101–1117. <https://doi.org/10.1175/JHM-D-15-0190.1>
- 827 Massari, C., & Maggioni, V. (2020). Error and Uncertainty Characterization. In V. Levizzani, C. Kidd, D. B.
828 Kirschbaum, C. D. Kummerow, K. Nakamura, & F. J. Turk (Eds.), *Satellite Precipitation*
829 *Measurement* (Vol. 69, pp. 515–532). Cham: Springer International Publishing.
830 https://doi.org/10.1007/978-3-030-35798-6_4
- 831 Moazami, S., & Najafi, M. R. (2021). A comprehensive evaluation of GPM-IMERG V06 and MRMS with
832 hourly ground-based precipitation observations across Canada. *Journal of Hydrology*, 594, 125929.
833 <https://doi.org/10.1016/j.jhydrol.2020.125929>
- 834 Molod, A., Takacs, L., Suarez, M., Bacmeister, J., Song, I.-S., & Eichmann, A. (2012). The GEOS-5
835 atmospheric general circulation model: Mean climate and development from MERRA to Fortuna.
- 836 Nguyen, P., Ombadi, M., Sorooshian, S., Hsu, K., AghaKouchak, A., Braithwaite, D., et al. (2018). The
837 PERSIANN family of global satellite precipitation data: a review and evaluation of products.
838 *Hydrology and Earth System Sciences*, 22(11), 5801–5816. <https://doi.org/10.5194/hess-22-5801-2018>
- 839 O, S., & Kirstetter, P. (2018). Evaluation of diurnal variation of GPM IMERG-derived summer precipitation
840 over the contiguous US using MRMS data. *Quarterly Journal of the Royal Meteorological Society*,
841 144(S1), 270–281. <https://doi.org/10.1002/qj.3218>
- 842 O, S., Foelsche, U., Kirchengast, G., Fuchsberger, J., Tan, J., & Petersen, W. A. (2017). Evaluation of GPM
843 IMERG Early, Late, and Final rainfall estimates using WegenerNet gauge data in southeastern Austria.
844 *Hydrology and Earth System Sciences*, 21(12), 6559–6572. <https://doi.org/10.5194/hess-21-6559-2017>

- 845 Petracca, M., D'Adderio, L. P., Porcù, F., Vulpiani, G., Sebastianelli, S., & Puca, S. (2018). Validation of GPM
846 Dual-Frequency Precipitation Radar (DPR) Rainfall Products over Italy. *Journal of*
847 *Hydrometeorology*, 19(5), 907–925. <https://doi.org/10.1175/JHM-D-17-0144.1>
- 848 Pierre-Emmanuel Kirstetter, Hong, Y., Gourley, J. J., Chen, S., Flamig, Z., Zhang, J., et al. (2012). Toward a
849 Framework for Systematic Error Modeling of Spaceborne Precipitation Radar with NOAA/NSSL
850 Ground Radar–Based National Mosaic QPE. *Journal of Hydrometeorology*, 13(4), 1285–1300.
851 <https://doi.org/10.1175/JHM-D-11-0139.1>
- 852 Randel, D. L., Kummerow, C. D., & Ringerud, S. (2020). The Goddard Profiling (GPROF) Precipitation
853 Retrieval Algorithm. In V. Levizzani, C. Kidd, D. B. Kirschbaum, C. D. Kummerow, K. Nakamura, &
854 F. J. Turk (Eds.), *Satellite Precipitation Measurement* (Vol. 67, pp. 141–152). Cham: Springer
855 International Publishing. https://doi.org/10.1007/978-3-030-24568-9_8
- 856 Sarachi, S., Hsu, K., & Sorooshian, S. (2015). A Statistical Model for the Uncertainty Analysis of Satellite
857 Precipitation Products. *Journal of Hydrometeorology*, 16(5), 2101–2117. [https://doi.org/10.1175/JHM-](https://doi.org/10.1175/JHM-D-15-0028.1)
858 [D-15-0028.1](https://doi.org/10.1175/JHM-D-15-0028.1)
- 859 Scheuerer, M., & Hamill, T. M. (2015). Statistical Postprocessing of Ensemble Precipitation Forecasts by
860 Fitting Censored, Shifted Gamma Distributions. *Monthly Weather Review*, 143(11), 4578–4596.
861 <https://doi.org/10.1175/MWR-D-15-0061.1>
- 862 Scheuerer, M., Hamill, T. M., Whitin, B., He, M., & Henkel, A. (2017). A method for preferential selection of
863 dates in the Schaake shuffle approach to constructing spatiotemporal forecast fields of temperature
864 and precipitation: SELECTING DATES IN THE SCHAAKE SHUFFLE. *Water Resources Research*,
865 53(4), 3029–3046. <https://doi.org/10.1002/2016WR020133>

- 866 Skofronick-Jackson, G., Petersen, W. A., Berg, W., Kidd, C., Stocker, E. F., Kirschbaum, D. B., et al. (2017).
867 The Global Precipitation Measurement (GPM) Mission for Science and Society. *Bulletin of the*
868 *American Meteorological Society*, 98(8), 1679–1695. <https://doi.org/10.1175/BAMS-D-15-00306.1>
- 869 Skofronick-Jackson, G., Kirschbaum, D., Petersen, W., Huffman, G., Kidd, C., Stocker, E., & Kakar, R.
870 (2018). The Global Precipitation Measurement (GPM) mission’s scientific achievements and societal
871 contributions: reviewing four years of advanced rain and snow observations. *Quarterly Journal of the*
872 *Royal Meteorological Society*, 144(S1), 27–48. <https://doi.org/10.1002/qj.3313>
- 873 Sorooshian, S., Hsu, K.-L., Gao, X., Gupta, H. V., Imam, B., & Braithwaite, D. (2000). Evaluation of
874 PERSIANN System Satellite–Based Estimates of Tropical Rainfall. *Bulletin of the American*
875 *Meteorological Society*, 81(9), 2035–2046. [https://doi.org/10.1175/1520-0477\(2000\)081<2035:EOPSSE>2.3.CO;2](https://doi.org/10.1175/1520-0477(2000)081<2035:EOPSSE>2.3.CO;2)
- 877 Sun, Q., Miao, C., Duan, Q., Ashouri, H., Sorooshian, S., & Hsu, K.-L. (2018). A Review of Global
878 Precipitation Data Sets: Data Sources, Estimation, and Intercomparisons. *Reviews of Geophysics*,
879 56(1), 79–107. <https://doi.org/10.1002/2017RG000574>
- 880 Tan, J., Petersen, W. A., & Tokay, A. (2016). A Novel Approach to Identify Sources of Errors in IMERG for
881 GPM Ground Validation. *Journal of Hydrometeorology*, 17(9), 2477–2491.
882 <https://doi.org/10.1175/JHM-D-16-0079.1>
- 883 Tan, J., Petersen, W. A., Kirstetter, P.-E., & Tian, Y. (2017). Performance of IMERG as a Function of
884 Spatiotemporal Scale. *Journal of Hydrometeorology*, 18(2), 307–319. <https://doi.org/10.1175/JHM-D-16-0174.1>
- 885

- 886 Tan, J., Petersen, W. A., Kirchengast, G., Goodrich, D. C., & Wolff, D. B. (2018). Evaluation of Global
887 Precipitation Measurement Rainfall Estimates against Three Dense Gauge Networks. *Journal of*
888 *Hydrometeorology*, 19(3), 517–532. <https://doi.org/10.1175/JHM-D-17-0174.1>
- 889 Tang, G. (2020). Characterization of the Systematic and Random Errors in Satellite Precipitation Using the
890 Multiplicative Error Model. *IEEE Transactions on Geoscience and Remote Sensing*, 1–10.
891 <https://doi.org/10.1109/TGRS.2020.3028525>
- 892 Tang, G., Ma, Y., Long, D., Zhong, L., & Hong, Y. (2016). Evaluation of GPM Day-1 IMERG and TMPA
893 Version-7 legacy products over Mainland China at multiple spatiotemporal scales. *Journal of*
894 *Hydrology*, 533, 152–167. <https://doi.org/10.1016/j.jhydrol.2015.12.008>
- 895 Tang, L., & Hossain, F. (2012). Investigating the similarity of satellite rainfall error metrics as a function of
896 Köppen climate classification. *Atmospheric Research*, 104–105, 182–192.
897 <https://doi.org/10.1016/j.atmosres.2011.10.006>
- 898 Tian, Y., Peters-Lidard, C. D., Eylander, J. B., Joyce, R. J., Huffman, G. J., Adler, R. F., et al. (2009).
899 Component analysis of errors in satellite-based precipitation estimates. *Journal of Geophysical*
900 *Research*, 114(D24). <https://doi.org/10.1029/2009JD011949>
- 901 Tian, Y., Huffman, G. J., Adler, R. F., Tang, L., Sapiano, M., Maggioni, V., & Wu, H. (2013). Modeling errors
902 in daily precipitation measurements: Additive or multiplicative?: MODELING ERRORS IN
903 PRECIPITATION DATA. *Geophysical Research Letters*, 40(10), 2060–2065.
904 <https://doi.org/10.1002/grl.50320>
- 905 Trinh, B. N., Thielen-del Pozo, J., & Thirel, G. (2013). The reduction continuous rank probability score for
906 evaluating discharge forecasts from hydrological ensemble prediction systems: Reduction continuous

- 907 rank probability score for HEPS. *Atmospheric Science Letters*, 14(2), 61–65.
- 908 <https://doi.org/10.1002/asl2.417>
- 909 Ushio, T., Sasashige, K., Kubota, T., Shige, S., Okamoto, K., Aonashi, K., et al. (2009). A Kalman Filter
910 Approach to the Global Satellite Mapping of Precipitation (GSMaP) from Combined Passive
911 Microwave and Infrared Radiometric Data. *Journal of the Meteorological Society of Japan*,
912 87A(November 2008), 137–151. <https://doi.org/10.2151/jmsj.87A.137>
- 913 Wilks, D. S. (2019). Forecast Verification. In *Statistical Methods in the Atmospheric Sciences* (pp. 369–483).
914 Elsevier. <https://doi.org/10.1016/B978-0-12-815823-4.00009-2>
- 915 Wright, D. B. (2018). Rainfall Information for Global Flood Modeling. In G. J.-P. Schumann, P. D. Bates, H.
916 Apel, & G. T. Aronica (Eds.), *Geophysical Monograph Series* (pp. 17–42). Hoboken, NJ, USA: John
917 Wiley & Sons, Inc. <https://doi.org/10.1002/9781119217886.ch2>
- 918 Wright, D. B., Kirschbaum, D. B., & Yatheendradas, S. (2017). Satellite Precipitation Characterization, Error
919 Modeling, and Error Correction Using Censored Shifted Gamma Distributions. *Journal of*
920 *Hydrometeorology*, 18(10), 2801–2815. <https://doi.org/10.1175/JHM-D-17-0060.1>
- 921 You, Y., Petkovic, V., Tan, J., Kroodsma, R., Berg, W., Kidd, C., & Peters-Lidard, C. (2020). Evaluation of V05
922 Precipitation Estimates from GPM Constellation Radiometers Using KuPR as the Reference. *Journal*
923 *of Hydrometeorology*, 21(4), 705–728. <https://doi.org/10.1175/JHM-D-19-0144.1>
- 924 Zhang, J., Howard, K., Langston, C., Kaney, B., Qi, Y., Tang, L., et al. (2016). Multi-Radar Multi-Sensor
925 (MRMS) Quantitative Precipitation Estimation: Initial Operating Capabilities. *Bulletin of the*
926 *American Meteorological Society*, 97(4), 621–638. <https://doi.org/10.1175/BAMS-D-14-00174.1>

927

**Toward A Globally-Applicable Uncertainty Quantification Framework for Satellite
Multisensor Precipitation Products based on GPM DPR**

Zhe Li¹, Daniel B. Wright¹, Samantha H. Hartke¹, Dalia B. Kirschbaum², Sana Khan^{2,3}, Viviana
Maggioni⁴, Pierre-Emmanuel Kirstetter^{5,6}

¹Department of Civil and Environmental Engineering, University of Wisconsin–Madison, Madison, WI, USA

²NASA Goddard Space Flight Center, Greenbelt, MD, USA

³Earth System Science Interdisciplinary Center, University of Maryland, MD, USA

⁴Civil, Infrastructure and Environmental Engineering Department, George Mason University, Fairfax, VA, USA

⁵School of Meteorology and School of Civil Engineering and Environmental Science, University of Oklahoma,
Norman, OK, USA

⁶NOAA/National Severe Storms Laboratory, Norman, OK, USA

Version: JUNE 07, 2021

Corresponding author: Dr. Zhe Li (zli875@wisc.edu)

Contents of this file

Tables S1

Figures S1 to S3

Table S1. The contingency tables for IMERG, benchmarked against GV-MRMS and 2BCMB. For each pair of the estimates, hits (top left), false alarms (top right), misses (bottom left), and correct non-detects (bottom right) are shown. The total paired data sample size over CONUS is 20,986,107.

	$P_{\text{IMERG}} \geq 0.1 \text{ mm h}^{-1}$	$P_{\text{IMERG}} < 0.1 \text{ mm h}^{-1}$
$P_{\text{GV-MRMS}} \geq 0.1 \text{ mm h}^{-1}$	714,440 (3.4%) ^a	444,222 (2.1%)
$P_{\text{GV-MRMS}} < 0.1 \text{ mm h}^{-1}$	437,897 (2.1%)	19,389,548 (92.4%)
$P_{\text{2BCMB}} \geq 0.1 \text{ mm h}^{-1}$	681,936 (3.2%)	301,416 (1.4%)
$P_{\text{2BCMB}} < 0.1 \text{ mm h}^{-1}$	470,401 (2.2%)	19,532,354 (93.1%)

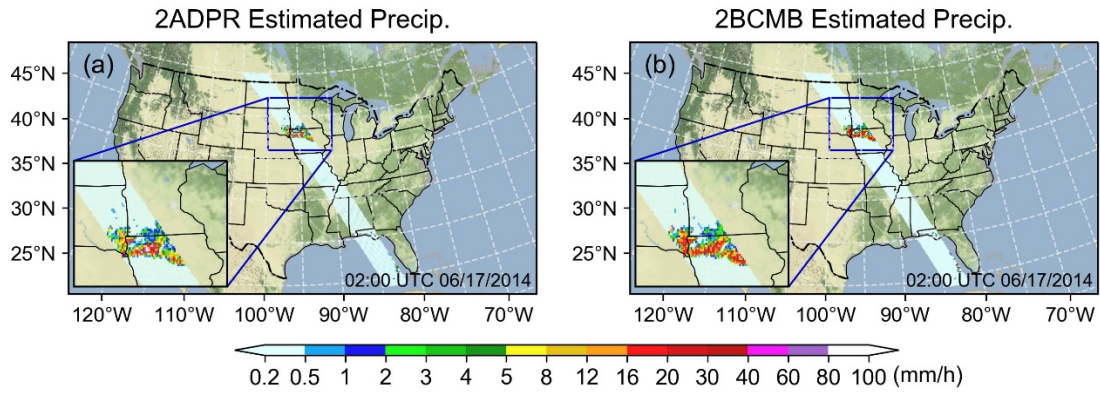


Figure S1. Coincident precipitation estimates from regridded (a) 2ADPR, and (b) 2BCMB for 02:00–03:00 UTC 17 June 2014. The swath coverage and retrieved precipitation spatial pattern of the two DPR derived products are similar, though 2BCMB shows enhanced precipitation intensities (which are closer to GV-MRMS observations, as shown in Figure 1b in the main article).

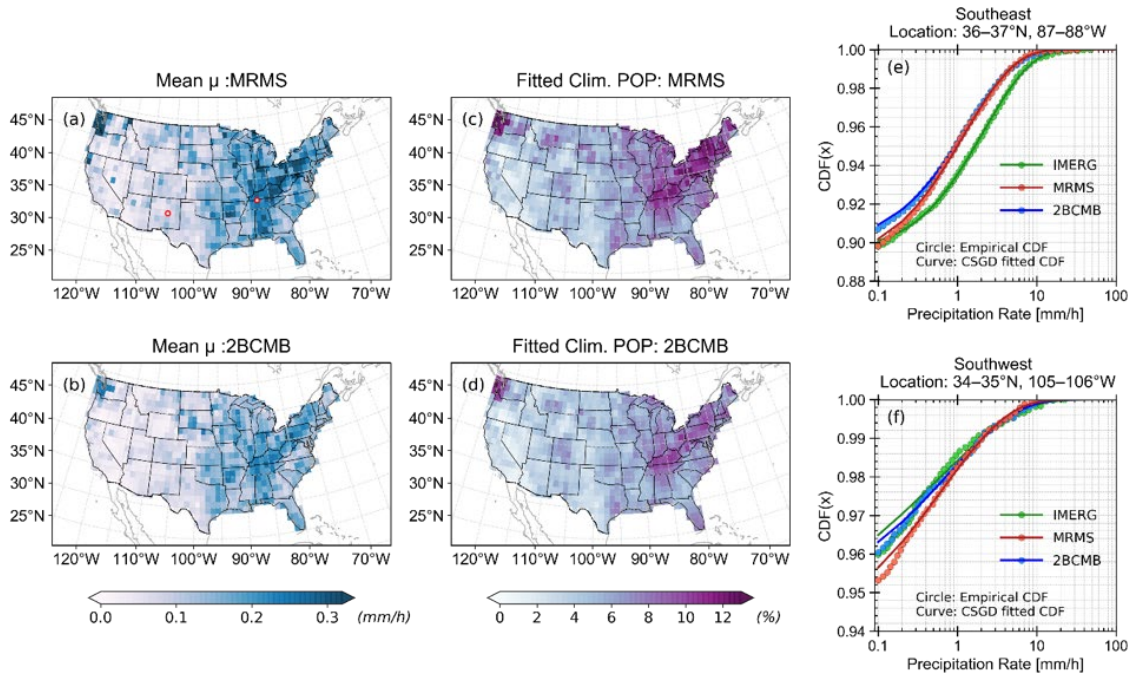


Figure S2. The spatial maps of fitted (a-b) climatological CSGD mean parameter μ and (c-d) POP, and (e-f) the comparison of empirical CDFs (markers) and climatological CSGD fitted CDFs (lines) based on the coincident IMERG, GV-MRMS, and 2BCMB training data samples within the $1^\circ \times 1^\circ$ boxes from the Southeast and Southwest CONUS, respectively. The locations of the two boxes are indicated by red circles in (a).

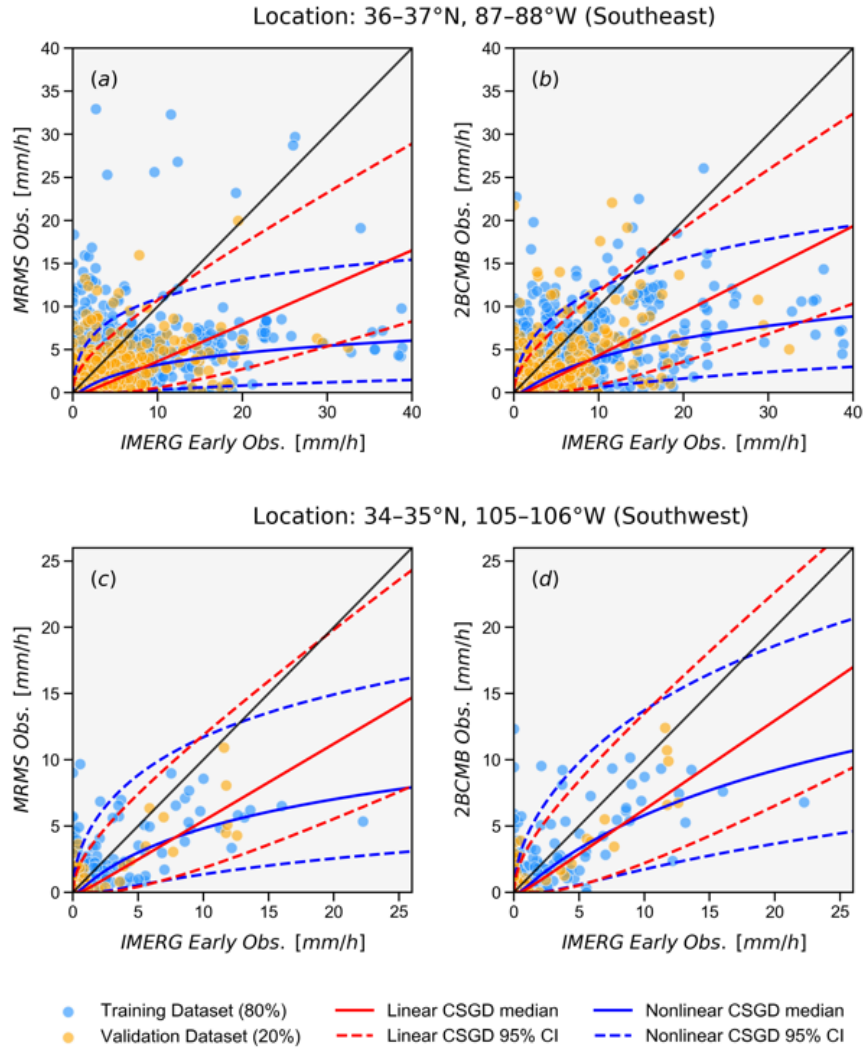


Figure S3. Linear (red lines) and nonlinear (blue lines) conditional CSGD models for (a, b) the Southeast $1^\circ \times 1^\circ$ box, (c, d) Southwest $1^\circ \times 1^\circ$ box, trained and compared against GV-MRMS (left panels) and 2BCMB (right panels). See Fig. 4 for identical results, but plotted on log scales.